EFFECT OF pH AND CALCINATION TEMPERATURE ON CO-PRECIPITATED INDIUM OXIDE NANOPARTICLES

GOH KIAN WEI

FACULTY OF ENGINEERING
UNIVERSITY OF MALAYA
KUALA LUMPUR

2017

EFFECT OF pH AND CALCINATION TEMPERATURE ON CO-PRECIPITATED INDIUM OXIDE NANOPARTICLES

GOH KIAN WEI

**DISSERTATION SUBMITTED IN FULFILMENT
OF THE REQUIREMENTS FOR THE DEGREE OF
MASTER OF ENGINEERING SCIENCE**

**FACULTY OF ENGINEERING
UNIVERSITY OF MALAYA
KUALA LUMPUR**

2017

ORIGINAL LITERARY WORK DECLARATION

Name of Candidate: **GOH KIAN WEI**

Registration/Matric No: **KGA 150038**

Name of Degree: **MASTER OF ENGINEERING SCIENCE**

Title of Project Paper/Research Report/Dissertation/Thesis ("this Work"):

Effect of pH and Calcination Temperature on Co-Precipitated Indium Oxide Nanoparticles.

Field of Study:

I do solemnly and sincerely declare that:

(1) I am the sole author/writer of this Work;
(2) This Work is original;
(3) Any use of any work in which copyright exists was done by way of fair dealing and for permitted purposes and any excerpt or extract from, or reference to or reproduction of any copyright work has been disclosed expressly and sufficiently and the title of the Work and its authorship have been acknowledged in this Work;
(4) I do not have any actual knowledge nor do I ought reasonably to know that the making of this work constitutes an infringement of any copyright work;
(5) I hereby assign all and every rights in the copyright to this Work to the University of Malaya ("UM"), who henceforth shall be owner of the copyright in this Work and that any reproduction or use in any form or by any means whatsoever is prohibited without the written consent of UM having been first had and obtained;
(6) I am fully aware that if in the course of making this Work I have infringed any copyright whether intentionally or otherwise, I may be subject to legal action or any other action as may be determined by UM.

Candidate's Signature Date:

Subscribed and solemnly declared before,

Witness's Signature Date:

Name:

Designation:

ABSTRAK

Zarah nano indium oksida (In_2O_3) telah berjaya disintesis dengan menggunakan kaedah pemendakan-bersama. Melalui kaedah pemendakan-bersama, zarah nano indium hidroksida ($In(OH)_3$) pada mulanya disintesis pada nilai pH 8, 9, 10 dan 11. Zarah nano In_2O_3 telah dibentuk daripada pengkalsinan zarah nano $In(OH)_3$ pada pelbagai suhu pengkalsinan (200, 300, 400, 500, 600 ℃). Ciri-ciri struktur sampel telah analisa oleh analisis gravimetrik termal (TGA dan DTA), pembelauan sinar-X (XRD), spektroskopi infra-merah jelmaan Fourier (FTIR), spektroskopi Raman, pengukuran potensi zeta, dan mikroskop penghantaran elektron beresolusi tinggi (HRTEM). Pengiraan nilai saiz zarah nano $In(OH)_3$ dan In_2O_3 menggunakan persamaan Scherrer mempunyai corak yang sama dengan nilai yang diperolehi daripada plot Williamson-Hall. Imej HRTEM menunjukkan bahawa saiz zarah nano $In(OH)_3$ adalah dalam lingkungan 11.76 - 20.76 nm. Sampel pH 10 mempunyai potensi zeta yang maksimum (3.68 mV) dan taburan saiz zarah yang paling kecil (92.6 nm). Oleh itu, kajian lanjut pada pembentukan zarah nano In_2O_3 telah dijalankan melalui pengkalsinan zarah nano $In(OH)_3$ pada nilai optimum pH 10. Kajian XRD, Raman, FTIR, TGA dan DTA telah menunjukkan bahawa zarah nano $In(OH)_3$ telah berjaya membentuk zarah nano In_2O_3 pada 300 ℃. Selain itu, imej HRTEM menunjukkan bahawa saiz zarah nano In_2O_3 adalah dalam lingkungan 14.67 - 27.67 nm. Pembentukan dan taburan zarah nano In_2O_3 yang paling kecil (14.67 nm) dan seragam telah ditunjukkan pada suhu pengkalsinan yang rendah iaitu 300℃. Berbanding dengan kajian terdahulu, kajian ini telah mengesahkan bahawa zarah nano In_2O_3 yang terbaik boleh diperolehi pada pH 10 dengan mengkalsinkannya dalam suhu yang agak rendah iaitu 300℃ melalui kaedah pemendakan-bersama.

ABSTARCT

Indium oxide nanoparticles (In_2O_3 NPs) were successfully synthesized by co-precipitation method. By using co-precipitation method, indium hydroxide nanoparticles ($In(OH)_3$ NPs) were initially synthesized at various pH values of 8, 9, 10 and 11. The In_2O_3 NPs were formed by calcining the optimized as-prepared $In(OH)_3$ NPs at various calcination temperatures (200, 300, 400, 500, 600 ℃). Structural characterizations of the samples were performed by thermogravimetric (TGA and DTA) analysis, X-Ray Diffractometer (XRD), Fourier transform infrared spectroscopy (FTIR), Raman spectroscopy, zeta potential measurement, and high-resolution transmission electron microscope (HRTEM). The crystallite sizes of as-prepared $In(OH)_3$ and In_2O_3 NPs were calculated by Scherrer equation had similar trend with values obtained from William-Hall plot. HRTEM images showed that the particles size of as-prepared $In(OH)_3$ were within the range of 11.76 - 20.76 nm. The maximum zeta potential (3.68 mV) of $In(OH)_3$ NPs associated with the smallest particle size distribution (92.6 nm) were occurred at pH 10. Hence, further work on formation of In_2O_3 NPs were conducted by calcining the as-prepared $In(OH)_3$ NPs at an optimum pH 10. XRD, Raman, FTIR and thermal studies of the samples revealed that the $In(OH)_3$ NPs were converted completely into In_2O_3 NPs at 300 ℃. Besides, HRTEM images showed that the particles size of In_2O_3 NPs was within the range of 14.67 - 27.67 nm. The smallest In_2O_3 NPs (14.67 nm) with homogenous particle distribution were formed at lower calcination temperature of 300℃. As compare to literatures, this work clearly confirmed that optimized In_2O_3 NPs could be obtained at pH 10 with a relatively low calcination temperature of 300 ℃ via co-precipitation method.

ACKNOWLEDGEMENTS

I recite my prayer to God for giving me good health, precious time and bright mind to accomplish my research studies. I would like to thank the University of Malaya (UM) for giving me an opportunity to study here. Besides that, I would like to further my thanks to the Head of Mechanical Engineering Department, Associate Prof. Dr. Mohd Faizul Bin Mohd Sabri who gave the permission to proceed and encouraged me to go ahead with my research studies. I also would like to express my gratitude to the Faculty of Engineering that has provided me with all the materials and equipments to carry on with my research project.

Not forgetting to express my deeply indebted to my respectful and helpful supervisors, Ir. Dr. Wong Yew Hoong and Prof Dr. Mohd Rafie Bin Johan for their help, stimulating suggestions and encouragement during this research studies. It would be difficult to complete my research studies without their guidance and support especially in the project resources, references and ideas. The supervision, constructive advices, valuable comments and inputs given truly help the progression and smoothness of my research.

Sincerely, thanks are extended to all academic and administrative staffs of the Department of Mechanical Engineering for all their help and supports. Also, I would like to thank the technical staffs from Nanotechnology and Catalysis Research Centre of the University of Malaya for zeta potential measurement services. Special acknowledgement to be given to Mr. Mohd Said Bin Sakat for his help in thermogravimetric analysis. Besides, I would like to thank the FA lab staffs from MIMOS Berhad for their provision of high resolution transmission electron microscopy

(HRTEM) service. A special thank is also given to Ms. Nadiah Binti Ghazali for Raman analysis characterization service.

A great appreciation is dedicated to colleagues-cum-friends, especially Goh Kian Heng, Hor Yuen Haw, Lei Zhen Ce, Aainaa Aqilah Binti Baharuddin, Hetherin, and Tan Chin Choo for all their assistance, wise ideas, and suggestions throughout this research. I also want to express my thanks to my family, especially my parents who gave me advices and encouraged me to overcome all the problems to finish this research and thesis.

Last but not least, I would like to contribute my gratitude to the financial assistance provided by University of Malaya via Graduate Research Assistantship Scheme (GRAS) and High Impact Research Grant (UM-HIR-MOHE-ENG-12), Postgraduate Research Fund (PPP) (Grant No.: PG328-2016A), University of Malaya Research Grant (UMRG) (Grant No.: RP013D-13AET) and Fundamental Research Grant Scheme (Grant No.: FP057-2016).

TABLE OF CONTENTS

CHAPTER 1: INTRODUCTION

CHAPTER 2: LITERATURE REVIEW

CHAPTER 3: MATERIALS AND METHODOLOGY

CHAPTER 4: RESULTS AND DISCUSSION

CHAPTER 5: CONCLUSION AND FUTURE RECOMMENDATIONS

LIST OF TABLES

LIST OF FIGURES

SELECTED LIST OF ABBREVIATIONS

TCOs : Transparent Conductive Oxides
In_2O_3 : Indium Oxide
$In(OH)_3$: Indium Hydroxide
H_2 : Hydrogen
CO : Carbon Monoxide
Cl_2 : Chlorine
NO_2 : Nitrogen Dioxide
ZnO : Zinc Oxide
NPs : Nanoparticles
1-D : One Dimensional
c- In_2O_3 : Cubic Indium Oxide
h-In_2O_3 : Hexagonal Indium Oxide
NH_3 : Ammonia
C_2H_5OH : Ethanol
H_2S : Hydrogen Sulfide
HCHO : Formaldehyde
Sn^{4+} : Tin Ion
Fe^{3+} : Ferric Ion
CAS : Chemical Abstracts Service
PVD : Physical Vapor Deposition
LAL : Laser Ablation in Liquid
OH^- : Hydroxyl Ions
H_3O^+ ; Hydronium Ions
H_2O : Water

H^+ : Hydrogen

AR : Analytical Grade

FWHM : Full Width at Half Maximum

W-H : Williamson-Hall

XRD : X-Ray Diffraction

ICSD : Inorganic Crystal Structure Database

HRTEM : High-Resolution Transmission Electron Microscopy

DTA : Differential Thermal Analysis

TGA : Thermogravimetric Analysis

FTIR : Fourier Transform Infrared Spectroscopy

ZP : Zeta Potential

IEP : Isoelectric Point

SELECTED LIST OF SYMBOLS

Nm : Nanometer

µm : Micrometer

^{o}C : Degree Celsius

cm^{-1} : Reciprocal Centimeters

% : Percentage

λ : Wavelength of Radiation Beam (nm)

d : Interplanar Spacing (nm)

Θ : Diffraction Angle

D : Crystallite Size (nm)

ε : Microstrain

β : Peak Width at Half Maximum Intensity (FWHM)

K : Scherrer Constant

Å : Angstrom

E_g : Band Gap Energy (eV)

J : Nucleation Rate (m^{5}J^{-1}mol^{-1})

E_s : Interfacial Energy

V_m : Molar Volume

V : Ion Number

k_b : Boltzmann Constant (J/K)

T : Absolute Temperature (K)

S : Supersaturation of Solution

CHAPTER 1

INTRODUCTION

1.1 Background

Nowadays, transparent conductive oxides (TCOs) as electrical conductive materials prepared by thin film technologies and used in many optoelectronic devices such as in gas sensors, biosensors, and solar cells had been studied for many years due to their high electrical conductivity at room temperature (Selvakumar et al., 2014). In recent years, many metal oxide nanostructures such as tungsten oxide (WO_3) (Cao et al., 2016; Tong et al., 2016), titanium oxide (TiO_2) (Tshabalala et al., 2016), indium oxide (In_2O_3) (Parast & Morsali, 2011; Tseng & Tseng, 2009) and copper oxide (CuO) (Lupan et al., 2016; Shao et al., 2014) have been studied due to its promising candidate for applications in electronic and optoelectronic devices. So far, the design and controllable synthesis of metal oxide nanostructures with a desired structure in terms of size and shape has not been realized (Liu et al., 2008; Zhuang et al., 2007).

Among metal oxide nanostructures, indium oxide nanoparticles (In_2O_3 NPs) act as transparent conductive oxides (TCOs) have been utilized in several applications especially gas sensor devices due to its unique properties such as high electrical properties and optical transparency in the visible region (Acacia et al., 2010; Donato et al., 2011; Selvakumar et al., 2014). In_2O_3 NPs are sensitive to O_2, O_3, CO, NO_2, fuels and organic solvents since In_2O_3 NPs revealed good dispersion properties, excellent electron transfer ability and large surface area (Ayeshamariam et al., 2013). Besides, In_2O_3 NPs can be prepared from $In(OH)_3$ precursor by dehydration process at high temperature (Song & Zhang, 2014; Wan et al., 2015; Zhu et al., 2008). $In(OH)_3$ especially in nanostructure form is an important wide band gap energy (E_g) (5.15 eV) semiconductor material (Avivi et al., 2000; Lei et al., 2006; Motta et al., 2010; Zhang et al., 2003). In_2O_3 also acts as a transparent semiconductor material with a wide band gap (E_g) having range of 3.55-3.75 eV (Chang, 2014). Preparation of In_2O_3 from dehydration of $In(OH)_3$ was a favorable method due to several advantages such as it is a simple process with desired morphological control and well maintained of macro-morphology of as-prepared $In(OH)_3$ during dehydration (Kim et al., 2014; Wan et al., 2015; Xu et al., 2006; Zhu et al., 2004).

In the past few years, indium hydroxide ($In(OH)_3$), indium oxide (In_2O_3), and indium oxyhydroxide (InOOH) were investigated intensively (Chang, 2014; Shi et al., 2008; Zhu et al., 2004; Zhuang et al., 2007). However, many of their properties are not clearly known. It was noticeable that synthesis parameters such as initial composition and synthesis methods were highly affecting the optical and electronic properties of In_2O_3 NPs (Chang, 2014; Tao et al., 2015). Basically, In_2O_3 is a dielectric material. However, high density of electrical charge carriers included oxygen vacancies and free electrons make In_2O_3 films to be conductive. The obtained conducting electrons in these particles from donor sites are associated with oxygen vacancies (Xu et al., 2008). Furthermore, preparation of In_2O_3 NPs at low cost with high simplicity, practical, fast reaction time and environmental friendly are the main challenge to industrial requirement (Chang, 2014).

In the past, there were many research work mainly focuses on the synthesis and characterization of In_2O_3 NPs with different types of precursors and/or synthesis methods (Bagheri et al., 2009; Seetha et al., 2009; Souza et al., 2009; Zhang et al., 2015; Zhou et al., 1999). Perez et al. (1998) showed that preparation of high defined morphology $In(OH)_3$ nanoparticles without use of any surfactants were synthesized by a novel peptization method. Recently, Lin et al. (2016) prepared indium complex precursors by urea-based homogeneous precipitation method. They showed that 1-D rods, 2-D disks and 3-D cubes of $In(OH)_3$ precursors were obtained and claimed that urea concentration influenced the morphology of the precursors particles. Zhang et al. (2015) had used low cost indium nitrate hydrate ($In(NO_3)_2.4.5H_2O$) as precursor to prepare In_2O_3 NPs by sol gel method and characterized their structure and electrical properties. Souza et al. (2009) had synthesized In_2O_3 NPs by a surfactant-free room temperature soft chemical route and studied their thermal, structural, microstructural and optical properties. Bagheri et al. (2009) reported on preparation and study of the structural properties of In_2O_3 NPs synthesized by both sol-gel and hydrothermal methods. To date, there is no report on the effect of high pH values (8, 9, 10 and 11) and different calcination temperatures (200, 300, 400, 500, and 600 ^{o}C) on the structural properties of $In(OH)_3$ NPs via co-precipitation method.

Herein, this work was focus on the synthesis of $In(OH)_3$ NPs via co-precipitation method at pH 8, 9, 10 and 11. The influence of pH on the surface morphology, microstructures, particle size, and phase transformation of $In(OH)_3$ NPs were investigated. Consequently, an optimum pH value was determined. Further work on conversion of as-prepared $In(OH)_3$ NPs to In_2O_3 NPs with optimum pH value by calcination process at 200, 300, 400, 500, and 600 ^{o}C was conducted and characterized.

1.2 Problem Statement

It is well known that the final geometry features of the In_2O_3 NPs are predetermined by the morphology and particles size of the $In(OH)_3$ NPs (Hu et al., 2009). Under optimal conversion conditions, cubic structure of $In(OH)_3$ precursor was pyrolyzed into cubic In_2O_3. Recently, $In(OH)_3$ NPs have been prepared by various chemical and physical synthesis methods including hydrolysis (Zhang et al., 2003), hydrothermal (Tavares et al., 2014; Zhu et al., 2004), solvothermal (Zhu et al., 2004), sol-gel (Tavares et al., 2014) and microwave irradiation (Liu et al., 2008). However, these synthesis routes require high temperature and take longer reaction time to form $In(OH)_3$ NPs (Li et al., 2011). Moreover, sol-gel, hydrothermal, co-precipitation, and solvothermal techniques are using inorganic salts as the main precursor to produce $In(OH)_3$ NPs (Chang, 2014; Motta et al., 2010; Zhu et al., 2004). Among them, co-precipitation method has the advantages due to its simple process (Li et al., 2006; Li et al., 2015; Safi et al., 2015; Zheng et al., 2015), low cost (Li et al., 2006; Safi et al., 2015), better homogeneous size of NPs (Li et al., 2015; Sathish, Shekar et al., 2014) and lower synthesis temperature (Gupta et al., 2011; Tang et al., 2003). The nucleation and growth of NPs can be controlled during synthesis process through this method forming more homogeneity sample (Zheng et al., 2015).

The characteristics of co-precipitate method such as the pH values and calcination temperatures can be varied to change the structural properties of the NPs to be synthesized. The pH values of the solution are one of the factors that will affect the crystallite size, morphology and crystallite phase of the In_2O_3 nanostructure. Although numerous investigations have been focused on the synthetization and characterization of In_2O_3 NPs, only few researchers work are related with pH values on the crystal size of In_2O_3 NPs (Hu et al., 2009; Tahar et al., 1997; Wang et al., 2009). The different pH values in the precursor solution affect the size of $In(OH)_3$ nanocube and subsequently react with oxygen to form In_2O_3 NPs had been reported by the Hu et.al (2009). They demonstrated that the size of the of $In(OH)_3$ nanocube decreased from 89 to 42 nm as the pH value increased from 10 to 12 and their shapes were still remained. They believed that the OH^- could also be a surfactant instead of only as a nucleation agent and subsequently react with oxygen to form In_2O_3 NPs. As similar study by Zhang et al. (2004) revealed that pH values of the precursor solution have a certain influence on the morphology of the NPs.

Indeed, the nucleation and growth of In_2O_3 NPs are strongly depending on the pH values. Results reported in the literatures demonstrated that pH values have been observed to influence the rate of ionic motion and chemical potential in the precursor solution (Hu et al., 2009). As a consequence, the different morphologies of the In_2O_3 NPs will be formed. In the case of $In(OH)_3$ NPs precursors, fast nucleation rate was observed at high pH values above 7. This is because of high concentration of hydroxyls obtained from the precursor solution causing faster reactions of In^{3+} ions with OH^- ions. Hence, formation of higher amount of crystal nuclei resulting the formation of small size of cubic $In(OH)_3$ NPs. By contrast, pH values below 7, fast crystal growth leads to formation of large crystal size due to low concentration of hydroxyls (Addonizio et al., 2014; Han et al., 2006). On the other words, different particles size of $In(OH)_3$ NPs were found associated with the competition between the crystal nucleation and growth (Ovanesyan et al., 2016). When the pH of the solution increased, the crystallite size of NPs is increased (Amirsalari & Shayesteh, 2015).

Furthermore, the calcination temperature is another key factor that must be controlled carefully since it might affect the morphologies, crystalline phase and particle size of the In_2O_3 NPs during synthesis process (Amirsalari & Shayesteh, 2015; Gu et al., 2014; Jin et al., 2011; Zhang et al., 2015). Calcination process is a process of remove water (H_2O) and hydroxide (OH) groups in the as-prepared $In(OH)_3$ precursors. This phenomenon leads to transitional of indium structures influencing the performance of the In_2O_3 NPs for several applications. Much efforts have been carried out to study the structural phase transition of In_2O_3 NPs by heat treated $In(OH)_3$ NPs at different calcination temperature (Zhang et al., 2015). It has been observed that the smaller grains tend to agglomerate to form a larger particles size when the calcination temperature increased. Selvakumar et al. (2014) had prepared In_2O_3 NPs by hydrothermal method at two different sintering temperatures (400℃ and 600℃). Based on the experimental results obtained, the crystallite size of In_2O_3 NPs was increased from 15 to 40 nm after annealed at 400℃ and 600℃, respectively.

1.3 Research Objectives

This study focuses on the following objectives:

i) To synthesize In_2O_3 NPs using co-precipitation method.

ii) To characterize the structure properties of as-prepared $In(OH)_3$ NPs at different pH values (8, 9, 10, and 11).

iii) To characterize the structure properties of In_2O_3 NPs with different calcination temperatures (200, 300, 400, 500 and 600℃).

1.4 Scope of study

In our research work, the In_2O_3 NPs are synthesis by co-precipitation method. In co-precipitation method, the $In(OH)_3$ NPs are initially prepared. Subsequently, conversion of as-prepared $In(OH)_3$ NPs into In_2O_3 NPs are done when the dehydration of as-prepared $In(OH)_3$ NPs are conducted at high temperature. There are two parameters performed in this study. The first parameter is the effect of different pH values (8, 9, 10, and 11) on the structure properties of as-prepared $In(OH)_3$ NPs. The second parameter is the effect of different calcination temperature (200, 300, 400, 500 and 600℃) on the structure properties of In_2O_3 NPs.

Several characterization techniques are conducted in order to investigate the structure properties of the as-prepared $In(OH)_3$ NPs and In_2O_3 NPs included the thermogravimetry (TG) analysis, differential thermal analysis (DTA), high resolution transmission electron microscopy (HRTEM) analysis, X-ray diffractometer (XRD) analysis, Fourier transform infrared (FTIR) spectroscopy, Raman analysis and Zeta potential analysis.

1.5 Thesis outline

This dissertation is organized in the following manner. Chapter 1 introduces the overview of the background study, problem statement, research objectives and scope of the study. Chapter 2 represents the literature review of some background theory in this study. Chapter 3 describes the systematics methodology of research work which includes the materials used, experimental procedures and characterization techniques. The following Chapter 4 focuses on analysing and interpreting the experimental results obtained. Last but not the least, conclusion and recommendation for future work are summarize in Chapter 5.

CHAPTER 2

LITERATURE REVIEW

2.1 Introduction

During the past decades, many metal oxide nanostructures had been investigated such as titanium oxide, indium oxide, copper oxide, and tin oxide (Exarhos & Zhou, 2007; Selvakumar et al., 2014). These metal oxide nanostructures had been investigated in many real life high technology applications including solar cells, gas sensor, flat panel display and low emissivity windows in order to improve the life quality of the human being (Golan et al., 2007; Lau et al., 2015; Minami, 2008). Hence, the structure properties of different metal oxide materials must be further investigated so that it is able to optimize the performance of the various applications. In the past few years, indium hydroxide ($In(OH)_3$), indium oxide (In_2O_3), and indium oxyhydroxide (InOOH) were investigated intensively due to their novel optical and electrical properties (Chang, 2014; Liu et al., 2008; Shi et al., 2008; Tao et al., 2015; Tseng & Tseng, 2009; Zhang et al., 2015; Zhu et al., 2004; Zhuang et al., 2007). In_2O_3 NPs acts as transparent conductive oxides (TCOs) were selected for our research since their properties are not fully explored. It is well known that preparation methods and precursors of In_2O_3 are highly affecting the structure properties such as morphology, particle shape and size of In_2O_3 NPs (Garkova et al., 2006; Tao et al., 2015). The design and controllable synthesis of In_2O_3 NPs with a desired structure in terms of size and shape is still a challenge (Zhuang et al., 2007). Therefore, it is necessary to review the literatures of synthesized In_2O_3 NPs prepared by different synthesize routes and conditions and their structure properties are summarized in this chapter.

2.2 Indium oxide nanoparticles (In_2O_3 NPs)

Indium oxide (In_2O_3) is an important transparent conductive semiconductor with a wide direct and indirect band gaps (E_g) of about 3.6 and 2.6 eV, respectively (Choi et al., 2009; Yang et al., 2011; Yang et al., 2010). In_2O_3 is an insulator in its stoichiometric state but becoming highly conductive in non-stoichiometric state which make it high reflectivity and high transparency in the infrared and visible light range, respectively. In the recent years, synthesis of the indium oxide (IO) or indium tin oxide (ITO) in bulk and thin film form has been performed by many researches since it has achieved considerable attentions as a favourable material for a variety of applications such as gas sensors, solar cell and UV lasers (Guoa et al., 2011; Lewis & Paine, 2000; Wang et al., 2009). Among these applications, In_2O_3 is highly selected as a suitable material for gas sensing applications (Gurlo et al., 1997; Gurlo et al., 1997; Korotcenkov et al., 2004). When In_2O_3 is exposed to various gaseous, it can adjust its electrical conductance. Hence, In_2O_3 has been studied as chemical sensors for a long time for detecting H_2, CO, CI_2 and NO_2 (Lin et al., 2015). Jiao et al. (2003) showed that the In_2O_3 had high gas sensing response to low concentration of NO_2 but low sensitivity against deoxidizing gases. In_2O_3 films in H_2 gas sensor had shown good sensitivity and selectivity to CO reported by Chung et al. (2001).

Over the past decades, much In_2O_3 nanostructures as well as the one dimensional (1-D) nanostructures such as nanoparticles, nanowires, nanorods and nanobelts have been prepared due to its novel optical and electronic properties (Gao & Wang, 2006; Guoa et al., 2011; Hu et al., 2009; Kuo et al., 2005). In_2O_3 NPs are high conducting material. The conducting electrons of these particles are obtained from the donor sites associated with oxygen vacancies (Ayeshamariam et al., 2013). In addition, In_2O_3 NPs have good dispersion properties, excellent electron transfers ability and large surface area (Chang, 2014; Shi et al., 2008; Zhu et al., 2004). In the literatures, lot of research works reported that metal oxide NPs such as aluminium oxide (Al_2O_3), chromium oxide (Cr_2O_3) and zinc oxide (ZnO) NPs can be obtained by dehydration of the corresponding metal hydroxide in air at high temperature (Chithra et al., 2015; Kohli et al., 2011; Mitsui, Matsui et al., 2009; Naono & Nakai, 1989). As similar to In_2O_3 NPs, dehydration of as-prepared indium hydroxide ($In(OH)_3$) NPs allow it convert into In_2O_3 NPs. In addition, the desired morphologies of In_2O_3 NPs can be formed by controlling the morphologies of the as-prepared $In(OH)_3$ NPs (Song & Zhang, 2014; Zhu et al., 2004; Zhuang et al., 2007). This is because In_2O_3 NPs enable to inherit their morphologies during the dehydration process. Meanwhile, it was believed that the structure properties of the In_2O_3 NPs are depend upon on the as-prepared $In(OH)_3$ NPs (Amirsalari & Shayesteh, 2015). Formation of In_2O_3 NPs by dehydration of as-prepared $In(OH)_3$ NPs is selected as a favourable method due to its advantages such as desirable morphology of as-prepared $In(OH)_3$ NPs can be easily obtained by aqueous phase method and the original morphology of the as-prepared $In(OH)_3$ NPs is maintained after calcination (Guoa et al., 2011; Kim et al., 2014).

2.2.1 Crystal phase of In_2O_3 NPs

Basically, there are two phases of In_2O_3 which are the cubic bixbyite-type structure In_2O_3 (c-In_2O_3) and hexagonal corundum type structure In_2O_3 (h-In_2O_3) (Wang et al., 2009). It is necessary to understand the phase transition of In-O system as well as the stability of different structure of In_2O_3 due to its importance in various applications fields (Gurlo et al., 2008). In general, In_2O_3 crystallites are usually in the cubic bixbyite-type structure under normal condition. C-In_2O_3 consists of space group Ia_3 and the cell contains 16 units (Epifani et al., 2004; Gurlo et al., 2003; Gurlo et al., 2008). For hexagonal corundum type structure h-In_2O_3, it is formed by conversion of c-In_2O_3 under high pressure and/or temperature and consists of space group R_3c and the cell contains 6 units (Epifani et al., 2004; Gurlo et al., 2008; D. Liu et al., 2008). A sequence of phase transitions from cubic to monoclinic and lastly into hexagonal of In_2O_3 will take place under high pressure. The conversion of c-In_2O_3 into h-In_2O_3 is reconstructive where a large kinetic energy barrier is present (Guo et al., 2008; Liu et al., 2008; Meyer et al., 1995). In fact, In_2O_3 is usually present in a transition sequence from cubic into hexagonal instead of going through monoclinic structure. Figure 2.1 represents the crystal structure of c-In_2O_3 and h-In_2O_3. Two different types of indium (In^{3+}) ions occupied the trigonal and octahedral prismatic interstices within the lattice of O^{2-} ions where oxygen (O) atoms are located at 8b, 24d and 48e Wyckoff positions as shown in Fig. 2.1(a). On the other hand, Fig. 2.1(b) shows that h-In_2O_3 contains only In^{3+} ions trigonal biprism within the lattice of O^{2-} ions where oxygen (O) atoms are occupying the 12c and 18e Wyckoff position (D. Liu et al., 2008). As a result, different phases of In_2O_3 with different properties will affect the performance various applications. For instance, Wang et al. (2009) reported that c-In_2O_3 NPs had higher gas sensing properties than the h-In_2O_3 microsphere in determination of ethanol (C_2H_5OH), ammonia (NH_3) gas and formaldehyde (HCHO). They revealed that small grain size of porous structure of c-In_2O_3 NPs enables the target gases molecules to deposit uniformly on the surface.

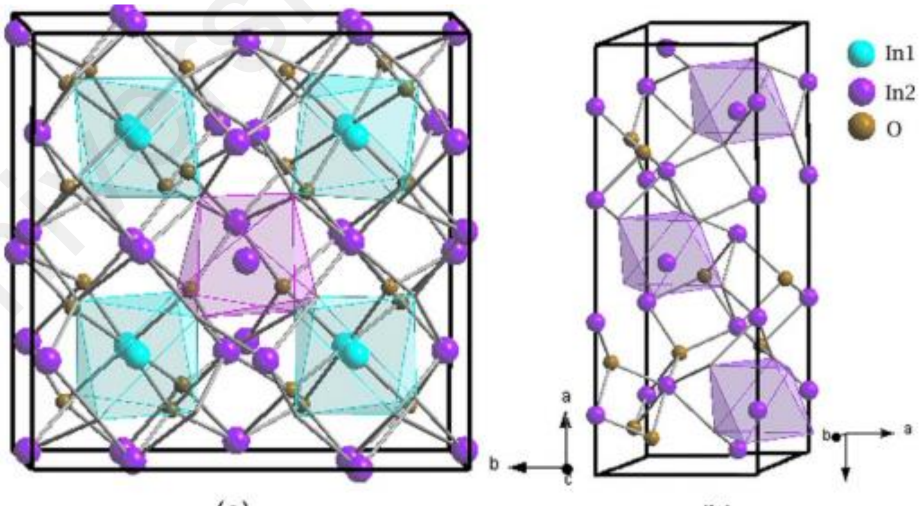

(a) (b)

Figure 2.1: Crystal structure of (a) c-In_2O_3; and (b) h-In_2O_3.

2.2.1.1 Cubic indium oxide (c-In_2O_3)

C-In_2O_3 can be defined as an oxygen-deficient fluorite structure (Epifani et al., 2004). Typically, In_2O_3 has been studied and utilized for most of the In_2O_3 products over the past decades including the one dimensional (1-D) In_2O_3 nanostructures were in the form of cubic structure (Jiang et al., 2004; Seetha et al., 2012; Xu et al., 2007; Xu et al., 2006). Jiang et al. (2004) have been synthesized porous structure of c-In_2O_3 nanowires by calcined the indium glycolate nanowires at 500℃ in air. C-In_2O_3 is the most stable form at ambient condition (Liu et al., 2008). Stabilization of the c-In_2O_3 increases its electrical conductance (Devi et al., 2002). Seetha et al. (2012) showed that c-In_2O_3 nanoparticles (40nm) prepared by hydrothermal route exhibits fast gas sensing response and recovery time towards ethanol vapours. C-In_2O_3 nanoparticles showed good sensing response toward 50 ppm of hydrogen sulfide (H_2S) at 268.5℃ prepared by Xu et al. (2006) via hydrothermal method under ambient pressure.

2.2.1.2 Hexagonal indium oxide (h-In_2O_3)

In the literature, the properties of metastable h-In_2O_3 were rarely investigated because of its difficulty in preparation. Previously, high temperature and high pressure are required to produce h-In_2O_3 nanostructures (Atou et al., 1990; Xu et al., 2008). For instance, Atou et al. (1990) reported that h-In_2O_3 was prepared by a shock-induced phase transition method under pressure of 15-25 GPa. Recently, many h-In_2O_3 nanostructures have been synthesized successfully under ambient pressure (Epifani et al., 2004; Lee et al., 2006; Xu et al., 2008). Lee et al. (2006) believed that h-In_2O_3 NPs might be synthesized at ambient pressure as if the dehydration of indium oxyhydroxide (InOOH) is very fast at low temperature can be achieved. They reported that the soluble and size controlled of h-In_2O_3 nanocubes have been synthesized successfully by surfactant assisted solution based methods at ambient pressure. Yu et al. (2003) have prepared the metastable h-In_2O_3 nanofibres by thermal dehydration of InOOH nanofibers precursors under ambient pressure. Besides, the conversion of cubic to hexagonal phase might accomplish if a smaller radius foreign atom of M such as Sn^{4+} and Fe^{3+} is inserted into the c-In_2O_3 network (Gurlo et al., 2003; Lee et al., 2006).

2.3 Synthesis method of In_2O_3 NPs

There are many methods that have been adopted for synthesis In_2O_3 NPs during the past decades (Gagaoudakis et al., 2001; Hu et al., 2003; Zhang et al., 2003). These different methods to synthesis In_2O_3 NPs are reported in the literatures including the physical and chemical processes. Physical processes are the physical vapor deposition (PVD), sputtering (Hu et al., 2003), and gas phase deposition (Gagaoudakis et al., 2001). Chemical processes are including sol-gel process (Shukla et al., 2004), hydrothermal method, laser ablation in liquid (LAL), mechanochemical reaction, solvothermal method, reverse microemulsion method and precipitate method (Li et al., 2006; Zhang et al., 2003). Moreover, the different preparation methods of indium oxide (In_2O_3) nanoparticles are slightly affect their structure, optical and electrical properties (Lau et al., 2015). All of these methods are also demanding in terms of costs, safety, energy and eco-compatibility.

2.3.1 Co-precipitation method

Co-precipitation method is a process of thermal decomposition of the precipitator to produce metal oxide NPs. Good crystallinity and excellent electrical conductivity of NPs can be obtained at lower synthesis temperature in co-precipitation method (Chen et al., 2014). On the other hand, it is regarded as an economy and simple way to synthesis In_2O_3 NPs (Gordani et al., 2016; Li et al., 2006; Vijayaprasath et al., 2016). $NH_3.H_2O$ and NH_3 are usually used as precipitants in co-precipitation method (Li et al., 2015). During thermal decomposition of precipitator, In_2O_3 NPs are produced uniformly in the solution and mono-dispersed. Hence, all NPs obtained should have almost similar properties (Xu & Yu, 2007). The co-precipitation process has been widely used to synthesis In_2O_3 NPs due to its purity and homogeneity which have possibility to control their particles shape and physical properties (Li et al., 2006; Xu & Yu, 2007). Besides, it was believed that particle size of In_2O_3 NPs is strongly depended by the reaction parameters including the pH and supersaturation in co-precipitation method (Wang et al., 2016). By controlling the nucleation and growth rate, desired size and distribution of In_2O_3 NPs are obtained during the synthesis process (Safi et al., 2016).

Kim et al. (2006) had reported on the preparation of In_2O_3 nanorods, nanoparticles and nanowires by co-precipitation and thermal evaporation methods. They found that about 100 nm diameters of both In_2O_3 nanoparticles and nanorods were obtained by co-precipitation method whereas In_2O_3 nanowires with 100 nm width and 2 µm length were obtained by thermal evaporation method. Besides, Li et al. (2006) had studied on the effect of annealing temperature on indium tin oxide (ITO) NPs synthesized by co-precipitation method. They reported that ITO powders with spherical and rod shapes were form at 600 ℃. Chithra et al. (2015) had investigated the effect of pH values on the optical properties and crystal size of zinc oxide NPs synthesized by co-precipitation method. They demonstrated that crystal size of zinc oxide NPs increased from 13.8 to 33 nm with increased in pH values of solution from 6 to 13.

2.3.2 Sol gel method

Sol-gel method is also known as wet chemical technique with subsequent heat treatment and it began to use in the 1800s (Forsh et al., 2014; Vasiliev et al., 2004). In sol-gel process, the precursor solution contains colloidal suspension of solid particles (~ 0.1-1 µm) in a chemical solution which act as the starting material to create the gel. A gel is a state of forming a solid network containing liquid components where both solid and liquid are dispersed with each other (Widodo & Sudrajad, 2015). Basically, metal alkoxides or metal chlorides are used as the starting material. Subsequently, they are undergoing hydrolysis and poly condensation reaction in an aqueous solution to form colloid. Small solid particles ranging between 1 nm to 1 μm in size are obtained in this colloid. Sol-gel process is believed as a reliable method to synthesis nanometer sized In_2O_3 (Widodo & Sudrajad, 2015). The size of In_2O_3 NPs obtained may lead to change on its structural and physical properties.

However, preparation method of In_2O_3 NPs is affected with some factors such as annealing temperature, solvent, and precursor concentration (Ayeshamariam et al., 2013; Flores-Mendoza et al., 2008; Forsh et al., 2014). For instance, an investigation on effect of annealing temperature on the properties of un-doped indium oxide studied have been reported by Flores-Mendoza et.al (2008). The grain size of indium oxide increased from 13-20 nm as the first annealing temperature increased. They expected the grains will coalesce when temperature was increased. Furthermore, the samples with first annealed in air at 300℃ and subsequently second annealed at 500℃ has the highest conductivity value of 10^2 $(\Omega\ cm)^{-1}$. Widodo (2015) also used the same preparation method to produce nanometer scale of uniform indium oxide particles about 100 nm. They believed that the nanosized particles of indium oxide with large surface area will be more sensitive to the gas sensors. Besides, Cantalini et al. (2000) studied the different preparation method sol-gel and vacuum thermal evaporation of indium oxide response to NO_2. Highly crystalline spherical nanoparticles and porous microstructure with average size of 19 nm were produced by sol-gel method while thermal evaporation produced denser and coalescent grain.

2.3.3 Laser ablation in liquid (LAL)

Laser ablation in liquid is novel method to produce metal oxide nanoparticles in the form of colloidal as well as in powder form. It is also known as wet physical technique (Donato et al., 2011; Sasaki et al., 2006). Laser ablation in liquid had been conducted by many researchers to investigate the formation of oxide NPs from pure metal in water. They indicated laser ablation in liquid is a reliable chemical reduction technique (Acacia et al., 2010; Tsuji et al., 2005). However, the shape and size of NPs are still depending on the several parameters including laser fluence and frequency, pulse width, repetition rate and height of the liquid above the target surface (Acacia et al., 2010). In addition, the size and aggregation state of NPs can be controlled by adding surfactants into the chemical solution (Donato et al., 2011; Gondal et al., 2010). Donato et al. (2011) prepared the In_2O_3 NPs by laser ablation in liquid used for CO sensing devices using indium as the precursor. The In_2O_3 NPs obtained was spherical in shape with a diameter around 20 nm. Acaci et al. (2010) also using the laser ablation technique to synthesis In_2O_3 NPs with varying the laser fluence and ablation time. They reported the present of NPs aggregation in the sample with nanosize below 20 nm and believed that the increment of NPs number is associated with high laser fluences and longer ablation time.

2.3.4 Reverse microemulsion method

Reverse microemulsion is also known as water-in-oil microemulsion where spheroidal aggregates are form when the surfactant molecules are dissolved in organic solvents. A monolayer of surfactant molecules is surrounded by dispersed aqueous phase microdroplets of less than 1 μm in oil phase (Kim et al., 1999; Lee et al., 2000). Reverse microemulsion also can be defined as reverse micelles. It can be form in presence or absence of water. In the presence of water droplets, the surface texture of aggregate is large and vice versa. In fact, water droplets act as the nanoreactors that enable chemical reaction to take place and in particularly can be used to synthesis inorganic NPs. On the other hand, monolayer of surfactant provides a barrier preventing the continuous growth of particles (Malik et al., 2012; Trotta et al., 1996). Thus, the formation of particles is limited within the dispersed water droplets as shown in Figure 2.2. In recent years, synthesis of nanoparticles by reverse microemulsion had been carried out and characterized by other researchers (Gan et al., 1996; Lopez-Quintela, 2003).

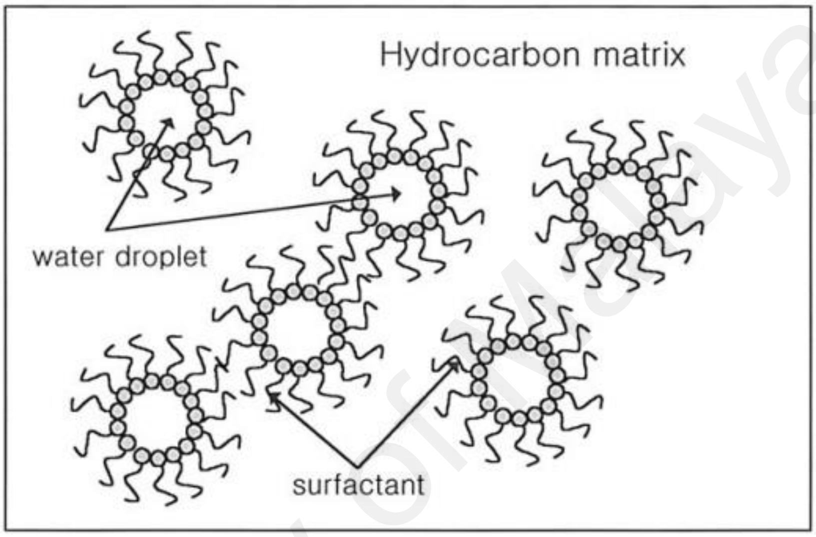

Figure 2.2: Synthesis of inorganic NPs by reverse microemulsion of dispersed water droplets in hydrocarbon (Lee et al., 2000).

Many metal oxide nanoparticles instead of indium oxide had been produced via the water-in-oil microemulsions technique including titania, tin oxide and indium tin oxide (Kim et al., 1999; Song & Kim, 1999; Stathatos et al., 1997). Zhan et al. (2004) had studied the formation of nanometer size In_2O_3 NPs using reverse microemulsion technique. From the results obtained, they revealed that the calcination temperatures will affect the size of In_2O_3 NPs. The average size of In_2O_3 NPs was increased gradually from 7 to 40 nm with increased in calcination temperature from 400 to 800℃.

2.3.5 Solvothermal method

Solvothermal method is a process used to produce single crystals in an autoclave at high temperature. It was typically similar to the hydrothermal method but there is only one difference which is the type of precursor solution. The precursor solution used in solvothermal solution usually is non-aqueous solution. However, there are two major factors may affect the production of small size In_2O_3 NPs with solvothermal method which are the presence of water and inorganic anions. Excess water causes aggregation of nanocrystals since water could acts as binder. Inorganic anions such as NO_3^- or CI^- can lead to aggregation of nanoparticles. Thus, proper control amount of water and use of suitable precursor could lead to synthesis monodisperse In_2O_3 NPs (Fan et al., 2012; Lin et al., 2015). Hu et al. (2009) used the solvothermal method to synthesis the In_2O_3 nanocubes by varying pH values. They reported that diameter of In_2O_3 nanocubes were decreased from 89 to 42 nm as the pH value increased from 10 to 12 whilst their shape remained. Lin et al. (2015) also reported the synthesis of monodispersed In_2O_3 NPs by solvothemal method in ethylene glycol. They produced approximately 5 nm In_2O_3 NPs without using any surfactant.

2.3.6 Hydrothermal method

Basically, hydrothermal method is a synthesis route for In_2O_3 NPs which almost similar to solvothermal method through the reaction in an autoclave at high temperature. However, the precursor solution use in hydrothermal method is an aqueous solution. Among other synthetic methods that had been established for preparation of In_2O_3 NPs, hydrothermal synthesis is able to produce low aggregation, controllable morphology and high crystallinity of metal oxide nanoparticles (Selvakumar et al., 2014; Xu et al., 2006). However, hydrothermal method requires high operate temperature at above 100℃ since it involves action of water. Hence, high pressure is developed by such solutions in this method (Safi et al., 2016). Jiaqiang et al. (2006) reported that cubic form In_2O_3 NPs was successfully prepared by hydrothermal method with fine dispersion and average size around 50-80 nm. According to the Mohagheghi et al. (2009) which studied on synthesis of In_2O_3 NPs by sol-gel and hydrothermal method, they stated that hydrothermal method is better than sol gel method due to its uniform distribution of smaller size in the range of 3-20 nm of cubic-hexagonal mixed phase NPs were formed.

2.3.7 Physical vapor deposition (PVD)

Physical vapor deposition is one of the physical methods for synthesis of In_2O_3. It is a process of evaporation of desired metal and subsequently condensation of vaporized metal onto the substrate to form the metal oxide film. Jeong et al. (2004) were focused on synthesis indium oxide nanobelts without catalyst by using simple physical vapor deposition at low temperature from 600℃ to 850℃. They mentioned that among the several progresses to synthesis In_2O_3 nanobelts or nanowires, it was still difficult to produce indium oxide nanobelts or nanowires at low temperature without catalyst. However, they were successfully to synthesis In_2O_3 with diameter in the range of 20-200 nm and its length up to hundreds of micrometers.

2.3.8 Mechanochemical process

Mechanochemical process is an alternative synthesis method for the formation of nanosized material involving high energy mechanical process within the precursor powders and subsequently chemical reaction occurred. Basically, the precursor powders are milled using a conventional ball mill to produce nanocomposite mixture of starting materials. In this process, the repeat collision between the precursor powders make change in the structural and develop a large interfacial contact area within reactants that allow the chemical reactions to take place. Mechanochemical process is also known as solid state reaction (Cukrov et al., 2001; Dodd & McCormick, 2002). However, mechanochemical process has some disadvantages where it requires high operating temperature and long heating time (Lee et al., 2000). Yang et.al (2004) studied the particles size of In_2O_3 synthesized by mechanochemical process with different calcination temperature (400 to 600℃). The crystal size obtained was 25.3 nm at 400℃ and 28.2 nm at 600℃, respectively. They demonstrated that the size of indium oxide nanoparticles increased with increasing in calcination temperature.

2.4 Influential parameters

In the past, synthesis of In_2O_3 nanostructure with optimum chemical and physical properties for various applications was not well explored. According to some earlier work on synthesis and characterization of obtained In_2O_3 nanostructure, it was noticeable that different structure properties of In_2O_3 nanostructure such as its morphology, particle size and crystalline phase affect the performance of its applications such as gas sensors (Caruntu et al., 2010; Elouali et al., 2012; Gurlo et al., 1997; Xu et al., 2007). For instance, Xu et al. (2007) showed that h-In_2O_3 nanorods prepared by a soft chemical route were highly sensitive to H_2S and dilute ethanol which is a promising candidates as H_2S and ethanol sensors. Another experimental reported by Elouali et al. (2012) revealed that c-In_2O_3 NPs (14 nm) prepared by hydrothermal method used in sensor devices shown rapid response to ethanol.

Thus, most of the researchers believed that the several parameters such as pH values and reaction temperature can be varied conveniently (Athawale & Bapat, 2005; Selvakumar et al., 2014; Vaidya et al., 2007). This is because these parameters are possible to control the chemical and physical properties of the nanostructure in terms of their particles size, distribution of particles, morphology and crystalline phase.

2.4.1 pH values

Typically, NPs surfaces become charged when immersed in an aqueous medium due to the protonation or deprotonation reactions of the dissociable functional groups at the interface of solid or liquid (Barisik et al., 2014; Ovanesyan et al., 2016). Interaction between the surface charge and dissolved ions results in formation of electrical double layer around the charged NPs. Transport of NPs are strongly depending on the particles surface charge properties. Hence, ion-ion correlation in the solutions of charged NPs is much attractive due to its ability to generate net attractive forces between equally charged NPs (Barisik et al., 2014). The size and concentration of solvent molecules have influence the formation of ions layer. Meanwhile, the formation layer affects the mean electrostatic potential and ions density in the diffuse region. This will have an effect on the zeta potential behavior and the number of ions accumulated near the particles surface (Jonsson et al., 2005; Labbez et al., 2009). The number of H^+ or OH^- ions in the precursor solution determines the polymerization of the metal oxygen bonds (Houng et al., 2007; Yuan et al., 2014). Therefore, pH of precursor solution will affect its hydrolysis and condensation behavior during the chain process where this will influence the morphology of the metal oxide nanostructures.

It is well known that surface area of the metal oxide nanoparticles such as ZnO nanoparticles at pH value below 7 is to be higher than that the nanoparticles obtained at pH above 7. The polymerization rate is greater than the hydration rate when pH value is above 7 lead to larger of particles size. In contrast, the hydration rate is greater than polymerization rate at pH lower than 7 in which a straight chain network structure is formed and particles size will decrease (Chen et al., 1995; Liu et al., 1994). The hydrolysis reaction rate at low pH is governed by the hydronium ion (H_3O^+) in the solution as described in Eq. (2.1).

$$H_2O + H^+ \rightarrow H_3O^+ \tag{2.1}$$

In this reaction, rapid formation of H_3O^+ causes less amount of water in the solution. Sharma et al. demonstrated that the hydrolysis or condensation in low pH is controlled and selective (Sharma et al., 2002). Hence, linear polymers of metal are generated leads to small aggregates at the end of the polycondensation process. In addition, high concentration of hydronium ion at low pH causes the nucleation rate reduced (Hamada et al., 1993). For high pH value, the reaction is control by the hydroxyl ions (OH^-) which will attract toward the positive charge of metal element in the solution to form metal oxide bond (Wahab et al., 2009; Wahab et al., 2009). Thus, synthesis of $In(OH)_3$ NPs in base solution (pH values above 7) is sufficiently effective than in acidic solution (pH values below 7). Although OH^- ions concentration increases in the solution lead to initial growth of $In(OH)_3$ NPs, but due to high concentration of OH^- ions enable occurring of cyclization since the intermolecular reaction is higher than intramolecular reaction (Houng et al., 2007). The hydrolysis and condensation at high pH values is uncontrolled and unselective which lead to highly branched polymers. Subsequently, larger interconnected particles are also generated. The particles size at high pH value is larger than the one at low pH value (Wahab et al., 2009).

Many researchers are focusing on the different materials like ZnO nanoparticles by varying its pH values (Addonizio et al., 2014; Chand et al., 2012; Husain et al., 2015; Wahab et al., 2009; Yuan et al., 2014; Yuan et al., 2015). However, it is clear from the earlier report that few researchers claimed that particle size of ZnO NPs decreases with pH values and few researchers found that it increases with pH values. Mohammad et al. (2010) showed that the smaller size of ZnO NPs with spherical shape was obtained as the pH of solution increased from 8 to 11 (49.98 - 36.65 nm). Agglomeration of ZnO NPs occurred when $Zn(OH)_2$ sol was in an acidic and neutral phase during synthesis process as a result of lack of OH^- ions in the sol. ZnO NPs with pH value above 9 contained high concentration of OH^- ions. This will cause the dissolution of ZnO and reduces its crystallite size (Chand et al., 2012; Wahab et al., 2009; Yuan et al., 2014). Rani et al. (2008) were prepared ZnO powders using sol-gel method by varying the pH values from 6 to 11. They found that the hexagonal shape of ZnO at pH 9 had the largest crystallite size (14 nm) and crystallite size decreased to about 12 nm as further increment pH value to 11.

2.4.2 Calcination temperature

Calcination temperature is another factor that will affect the crystallite size, phase composition, surface morphology and crystallinity of the In_2O_3 NPs (Li et al., 2015; Zhang et al., 2015). Removal of water and hydroxyl (OH) groups of $In(OH)_3$ NPs lead to the change in structure properties of the In_2O_3 NPs (Amirsalari & Shayesteh, 2015). Thus, calcination process must be controlled since it may cause the $In(OH)_3$ NPs to come in contact with each other and become larger particles due to the inter-diffusion process occurred during calcination (Reddy et al., 2015). Condensation reactions of as-prepared $In(OH)_3$ NPs lead to the formation of inorganic networks containing rigid and strong metal-oxo-metal (M-O-M) bridges where the particles size will be increased (Reddy et al., 2015; Sajjia et al., 2012). Chen et al. (2010) showed that the average crystallite sizes of cerium oxide nanocrystals increased from 12 to 47 nm when the calcination temperature increased from 473 to 1273 K. Recently, Selvakumar et al. (2014) synthesized In_2O_3 NPs by hydrothermal method and calcined at 400, 500 and 600 ^oC. They found that crystallite size of In_2O_3 NPs increased with the increasing calcination temperature. However, it is still lack of investigation on the effect of different calcination temperature on the structural properties of In_2O_3 NPs.

Besides, it is well known that suitable calcination temperature of In_2O_3 NPs might lead to higher surface area and a larger amount of oxygen vacant and lattice oxygen which are able to improve the sensing properties of sensor devices (Jin et al., 2011). Furthermore, Gu et al. (2014) reported In_2O_3 NPs prepared via solvothermal method with different calcination temperatures (300 to 600℃). They found that the In_2O_3 NPs tend to coarsen and aggregate as the calcination temperature increased which causes its surface area gradually decreased. Moreover, they showed that In_2O_3 NPs calcined at 300℃ exhibited higher response to ethanol due to its higher quantity of chemisorbed oxygen. In contrast, lower response of In_2O_3 NPs calcined at 600℃ toward ethanol was observed because of donor defects. According to the paper reported by the Forsh et al. (2014), the In_2O_3 powders were prepared by sol-gel method and calcined at 300, 500 and 700℃. The small nanocrystal size and large surface area of In_2O_3 NPs of about 7-8nm and 100 m^2 g^{-1} were obtained after annealed at 300℃, respectively. They found that the conductivity of In_2O_3 NPs was decreased and the activation energy had increased with the reduction in nanocrystal size.

2.5 Summary

In this chapter, the literatures are focused on the synthesized of metal oxide nanostructures with different synthesize routes and conditions. A deep understanding on the formation of In_2O_3 NPs and their structure properties were reviewed. Synthesis and characterization of In_2O_3 NPs with different pH values and calcination temperatures using the co-precipitation method have not been reported elsewhere. In_2O_3 NPs have been widely use in the applications especially as gas sensor devices because of its high electrical properties and good dispersion properties. The parameters such as pH values, calcination temperature and synthesis methods were highly affecting the structural properties of In_2O_3 in terms of their particles size and morphology. Most of the researchers stated that the pH values and calcination temperature can be varied conveniently since they were possible to control the structure properties of In_2O_3 nanostructure. It is noticeable that synthesize the In_2O_3 nanostructure at higher pH values (>7) is more effective than at lower pH values (<7). Rapid form of hydronium (H_3O^+) ions in acid solution will reduced the nucleation rate where the small particles tend to grow into larger particles. In contrast, in base solution, the hydroxide (OH^-) ions were react directly towards the In^+ ions. High concentration of OH^- ions makes the rapid formation of smaller In_2O_3 nanostructure in the solution. In addition, a suitable calcination temperature also must be selected in aqueous phase method because the inter-diffusion of particles may occur at a higher temperature. The attachment of small particles was occurred and it became large particles. Besides, among various type of synthesis methods, co-precipitation method is the favorable method due to its controllable, economy, and simple way to produce homogeneity metal oxide nanostructures.

CHAPTER 3

MATERIALS AND METHODOLOGY

3.1 Introduction

This chapter is dedicated to the description of the experimental materials used and methods employed in our research work. The overview experimental procedures starting from the preparation work to the process of collecting, analysis and interpreting the results is presented in the flow chart as shown in Fig. 3.1. The types of materials used, synthesis process as well as the characterization techniques are also discussed in this chapter.

Several characterization techniques are employed in our research works in order to study on the structural properties of the samples. The chemical and structural characterization techniques are listed and summarized. These techniques include of thermogravimetry analysis (TGA), differential thermal analysis (DTA), high resolution transmission electron microscopy (HRTEM) analysis, X-ray diffractometer (XRD) analysis, Fourier transform infrared spectroscopy (FTIR), Raman spectroscopy and Zeta potential analysis. The details of the processing steps in this research are explained in the experimental procedure.

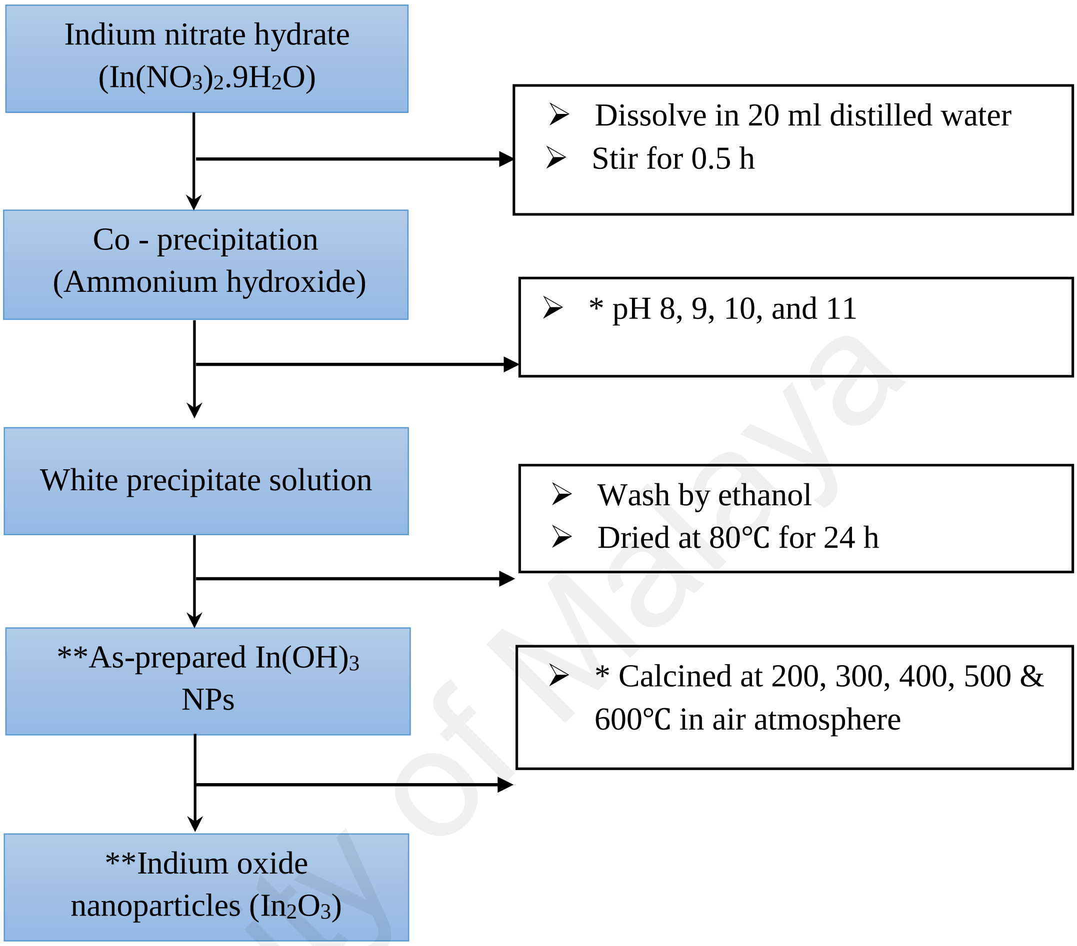

Remark:
*   Parameter that will be varied
**Characterize by TEM, XRD, FTIR, RAMAN, DSC/TG, PSD/ZP

Figure 3.1: Synthesis of In_2O_3 NPs and the characterization of the In_2O_3 NPs with different pH values and calcination temperatures.

3.2 Materials

In this present work, indium nitrate hydrate ($In(NO_3)_2.9H_2O$) as inorganic metal salt, ammonia hydroxide (NH_4OH), ethanol (C_2H_5OH) and distilled water were used as starting materials. All the materials used were analytical grade (AR) and without further purification. Indium nitrate hydrate is an inorganic metal salt and acts as the main precursor to produce $In(OH)_3$ NPs as well as In_2O_3 NPs. The chemical details of the starting materials include chemical formula, assay percentage and supplier with Chemical Abstracts Service (CAS) numbers are shown in Table 3.1.

Table 3.1: List of starting materials used for synthesis In_2O_3 NPs

No.	Materials	Chemical Formula	Assay (%)	Supplier / CAS No.
1.	Indium nitrate hydrate	$In(NO_3)_2.9H_2O$	99.9	Sigma-Aldrich / 207398-97-8
2.	Ammonia hydroxide	NH_4OH	25.0	Friendemann Schmidt / 1336-21-6
3.	Ethanol	C_2H_5OH	99.9	John Kollin / 64-17-5

3.3 Experimental Procedures

3.3.1 Synthesis of as-prepared $In(OH)_3$ NPs via co-precipitation method

Indium nitrate hydrate ($In(NO_3)_2.9H_2O$), ammonia hydroxide (NH_4OH), ethanol (C_2H_5OH) and distilled water were used as precursors. Firstly, 0.01 mol of $In(NO_3)_2.9H_2O$ was dissolved in 20 ml of distilled water and stirred magnetically for 0.5 h at room temperature. Then, NH_4OH in an aqueous solution was slowly dripped into the mixture and kept stirred magnetically until the solution became basic condition (pH 8). White precipitates were obtained and washed by ethanol and finally dried at 80℃ for 24 h. The similar process was also repeated at different pH values of 9, 10, and 11, respectively.

3.3.2 Conversion of $In(OH)_3$ NPs to In_2O_3 NPs

A similar processing steps were conducted to produce as-prepared $In(OH)_3$ NPs with an optimum pH 10. Once the pH value of translucent solution was adjusted to 10, the resultant white precipitates were then washed by ethanol and dried at 80℃ for 24 h. Finally, the anhydrous as-prepared white precipitates were calcined in a furnace at 200, 300, 400, 500 and 600 °C. A bright yellow of In_2O_3 NPs were obtained.

3.4 Characterizations Techniques

3.4.1 X-Ray Diffraction (XRD) analysis

X-ray powder diffraction (XRD) is a technique to characterize the crystallinity of the samples. Crystallinity of the sample is strongly depended upon the periodicity which is the long range order of the atoms or molecules in a particular sample (Venkateswarlu, Bose, & Rameshbabu, 2010). Here, the structure and phases purity of the samples can be analyzed or investigated by using XRD analysis (Mote et al., 2011; Sivakami et al., 2016). The diffraction process of X-Ray is described by Bragg's law.

$$\lambda = 2d\sin\theta \tag{3.1}$$

where λ is the wavelength of radiation beam (nm), d is the inter-planar spacing in a crystal (nm), and 2θ is the angle between the diffracted and the transmitted beams (°). This is achieved when the diffraction of X-Ray go through the lattice of atoms in a crystal. The XRD pattern of the samples with different diffraction peaks represented its crystallinity. The high intensity of diffraction peaks indicated a high degree of crystallization (Zhan et al., 2004).

In this present work, PANalytical Empyrean X-Ray diffractometer was used to study the crystalline phase of the samples in a scan rage of $2\theta = 10\text{-}90°$. Copper (Cu K_α) radiation ($\lambda = 0.15406$ nm) with an operating voltage of 45 kV and current of 40 mA was used as X-Ray source to identify sample crystallinity. XRD patterns of the sample with different peak intensity were recorded in a grazing incident X-Ray diffraction mode on PANalytical Empyrean X-Ray diffractometer. The intensity of diffraction peak against 2 θ was plotted after each sample was scanned.

Basically, XRD analysis allows evaluation of the diffraction peak broadening with crystallite size and microstrain of the samples as a result of the defect. The defect like the dislocation is one of the factor increased in crystallite size (D) and microstrain (ε) (Sivakami et al., 2016; Venkateswarlu et al., 2010). From this view of point, the crystallite size (D) and microstrain (ε) can be evaluated by three methods that are Fourier method, simplified Integral Breadth method, and double Voight method. Among them, simplified integral breadth method is able to give the average value of crystallite size instead of crystallite size distribution (Herrmann et al., 2009; Mittemeijer & Welzel, 2008; Vives et al., 2004). In general, there are two basic approaches in simplified integral breadth method that are Debye-Scherrer analysis and Williamson-Hall (W-H) analysis (Mittemeijer & Welzel, 2008; Mote et al., 2011).

3.4.1.1 Debye-Scherrer analysis

In this work, the crystallite size of the samples is estimated by using the Debye-Scherrer equation. The average crystallite size (D) from peak width (β_D) can be calculated by (Goh et al., 2016; Mote et al., 2011) :

$$D = \frac{K\lambda}{\beta_D \cos\theta} \tag{3.2}$$

where K is the Scherrer constant (0.9); λ is the wavelength of the radiation; ß$_D$ is the full width at half maximum intensity (FWHM); and θ is the peak position. All peak positions of the samples are extracted through Debye-Scherrer formula to determine its average crystallite size.

3.4.1.2 Williamson-Hall (W-H) analysis

Besides that, the crystallite value of the samples is also calculated using W-H models for comparison with values obtained from Scherrer formula and TEM analysis. W-H analysis allows estimating the crystallite size at various 2θ positions at one time as compare to Scherrer analysis only at single 2θ position. Meanwhile, defects such as distortions and imperfections generate strain in crystal resulting in peak broadening (Mote et al., 2011; Venkateswarlu et al., 2010). Thus, strain-induced broadening due to crystal imperfections and distortion can be expressed as:

$$\varepsilon = \frac{\beta_s}{4\tan\theta} \tag{3.3}$$

where β_s is the peak width at half maximum intensity (FWHM) and θ is the peak position. From the Eq. (3.2) and (3.3), it is confirmed that peak width from crystallite size inversely proportional to cos θ and strain inversely proportional to tan θ (Mittemeijer & Welzel, 2008; Mote et al., 2011). The crystallite size and strain are suitably calculated by using W-H analysis. In W-H analysis, we assumed that the two independent factors which one from the NPs scattering crystallite size (β size) and the other the microstrain (β strain) are contributed to the total peak broadening and both have Cauchy-like profile (convolution of Gaussian and Lorentzian profile) (Pandya et al., 2016). The total peak broadening is the summation of β arising from Sherrer equation (β_{D}) (Eq. (3.2)) and strain-induced broadening (β_s) (Eq. (3.3)) can be expressed as:

$$\beta_{hkl} = \beta_D + \beta_s \tag{3.4}$$

$$\beta_{hkl} = \frac{\kappa\lambda}{D\cos\theta} + 4\varepsilon\sin\theta \tag{3.5}$$

By rearranging the Eq. (3.4), W-H equation gives:

$$\beta_{hkl}\cos\theta = \frac{\kappa\lambda}{D} + 4\varepsilon\sin\theta \tag{3.6}$$

strain (ε) is the gradient of the graph and $\kappa/\lambda/D$ is the intercept of the graph where D can be calculated from the values.

3.4.2 Raman spectroscopy analysis

Raman spectroscopy is a commonly used technique to study chemical bonding stability of the samples. It is a reliable method because of its sensitivity of short range order such as cluster. This can be explained by the local order of cluster are structurally ununiformed can be distinguished due to their different types of electronic transitions and are linked to a specific structural arrangement (Kim et al., 2001; Motta et al., 2010). Raman spectrum is obtained by a change in polarizability during vibration. Furthermore, Raman spectroscopy can acts as denominator to differentiate the materials used by different groups when it comes to spectra interpretation (Ferrari, 2007). Therefore, Raman analysis is necessary to be used for phase identification and composition determination in our research work. The measurement of chemical bonding stability of the samples was employed by using Horiba Xplora One Raman spectrometer. Raman-scattering data was recorded in the range of 100-700 cm^{-1} by wavelength of 532 nm as excitation source from an Ar$^+$ laser beam.

3.4.3 FTIR spectroscopy analysis

FTIR analysis is a commonly used analytical technique applied to determine the presence of the specific chemical groups in the materials by absorption of infrared spectrum or emission of a material (Schmitt & Flemming, 1998). In general, FTIR is capable to provide qualitative and quantitative analysis for both organic and inorganic samples. It is well known that the information associated to the change in chemical bonding during crystal transformation as well as the amount of the components can be discriminate and identify by FTIR analysis (Oh et al., 2005; Yang et al., 2005).

In our work, the compositional analysis of the samples was conducted by a very useful vibrational spectroscopy technique using Perkin Elmer Spectrum 400 Fourier Transform infrared (FTIR) spectrometer. The FTIR transmittance spectrum in the range of 4000-400 cm^{-1} was used to determine the chemical functional groups present in the samples.

3.4.4 HRTEM analysis

HRTEM analysis is a microscopy technique which has been widely used to observe the surface morphology of samples. From this analysis, electron beam is emitted from the electron gun by Schottky, thermionic or filled emission (Yao et al., 2008). The interaction between the transmitted electrons and the sample surface produce an image. It is well known that the resolution power is depend on the sample thickness. Hence, the sample must be very thin (Zhang et al., 2006). A high magnification and resolution images that contain information down to few nanometers can be observed from the HRTEM analysis.

Consequently, the samples in this work were initially mixed with ethanol in a closed small glass tube. The closed glass tube was immersed in the ultrasonic bath for 15 minutes. A drop of mixture was then dropped onto the copper grid and left to dry in a few minutes. The samples were then analyzed by TECNAI G2 F20 high resolution transmission electron microscope (HRTEM). The microscope had accelerating voltage from 20 to 200 kV and standard magnification from 22 to 930 k.

3.4.5 Zeta potential analysis

Zeta potential analysis is used to characterize the electrostatic stabilization of the samples. The electrical potential of the interface between the aqueous solution and the stationary layer of ions attached to the particles is determined (de Vasconcelos et al., 2005; Fuerstenau & Pradip, 2005). Basically, the absolute value of positive and/or negative zeta potential more than 30mV is considered to form stable particles dispersions. This is because of the repulsion force exceeds the attraction force makes the particles repels with each other thus prevented them from agglomeration (Konkena & Vasudevan, 2012; Sankhla et al., 2016). Therefore, it is essential to measure the zeta potential of the samples in order to study the phenomena occurring at interface since modification of the surface charge was done by varying the pH values.

In this study, the surface charge and hydrodynamics size of samples are determined by Zetasizer Nano ZS analyzer (ZEN 3500, Malvern). This instrument measures the zeta potential and electrophoretic mobility of the samples based on dynamics light scattering. Before measurement, each sample was sonicated for 15 minutes prior to dispersion of the NPs in the aqueous solution. The data obtained was investigated using Zetasizer software.

3.4.6 TGA and DTA analysis

TGA and DTA analysis have been used to study on the weight composition and phase transformation of the samples (Seetha et al., 2009). In our research work, thermal decomposition behavior of the as-prepared samples was determined simultaneously by TGA and DTA analysis using a TGA/SDTA851 Ultramicro Balance (Mettler Toledo). The as-prepared samples were put into the aluminium crucible and heated from room temperature to 1000 ^{o}C under synthetic air flow subjected to a heating rate of 10 ^{o}C min^{-1}. The formation temperature and phase transformation of the as-prepared sample were represented in the TGA and DTA curve. The corresponding percentage weight losses and transition temperature were then plotted.

CHAPTER 4

RESULTS AND DISCUSSION

4.1 Introduction

This chapter presents the experimental results and discussion on the structural properties of the as-prepared In(OH)$_3$ NPs and In$_2$O$_3$ NPs synthesized by co-precipitation method. The discussion is basically divided into two main parts: (i) Effect of pH variation on the stability and structural properties of the In(OH)$_3$ NPs synthesized by co-precipitation method and (ii) Effect of calcination temperatures on the structural properties of the In$_2$O$_3$ NPs synthesized by co-precipitation method.

4.2 pH variation effects

As presented in Chapter 2, by using co-precipitation method, it is a simple and economical way to synthesis In$_2$O$_3$ NPs through thermal decomposition of the as-prepared In(OH)$_3$ NPs where similar structural and physical properties are maintained (Gordani et al., 2016; Li et al., 2006). pH is one of the reaction parameters that may affect their properties in co-precipitation method (Wang et al., 2016). Thus, In(OH)$_3$ NPs were synthesized at different pH values of 8, 9, 10 and 11 which has not been reported elsewhere.

4.2.1 X- Ray Diffraction (XRD) analysis

Figure 4.1 shows the typical XRD patterns of In(OH)$_3$ NPs synthesized under different pH values (8, 9, 10, 11) appeared with distinct diffraction peaks. It is clear that the cubic phase of In(OH)$_3$ NPs occurred at angles of 2θ = 22.7°, 29.2°, 33.1°, 40.1°, 45.8°, 51.3°, 56.8°, 66.5°, 75.5°, 71.0° and 80.0° with various planes of (200), (211), (220), (222), (400), (420), (422), (440), (442), (620) and (622), respectively. All diffraction peaks are indexed to cubic structure of $In(OH)_3$ NPs with lattice constant, a = 7.9743 Å. The XRD results are consistent with the Inorganic Crystal Structure Database (ICSD) with reference code 01-076-1463. The peaks are slightly decreasing from pH 8 to 10 but getting highest as the pH increases to 11. This may explained by the well-distribute of the cubic $In(OH)_3$ NPs at pH 11.

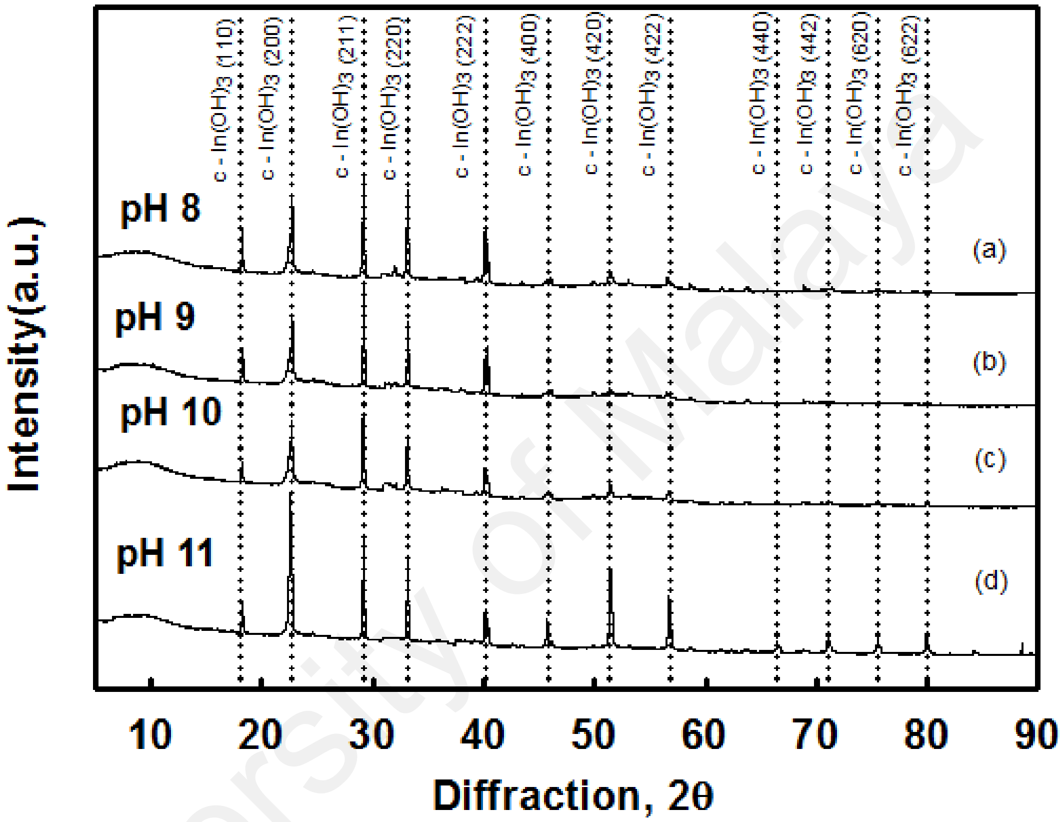

Figure 4.1: XRD patterns of as-synthesized $In(OH)_3$ NPs at different pH values: (a) 8; (b) 9; (c) 10 and (d) 11.

The crystallite size of the $In(OH)_3$ NPs was calculated by using Debye-Scherrer equation as shown in Eq.(3.2). All peaks of $In(OH)_3$ NPs were used to determine its average crystallite size. Figure 4.2 shows the average crystallite size of $In(OH)_3$ NPs for pH values of 8, 9, 10 and 11 are 15.42 nm, 16.34 nm, 11.04 nm, and 14.86 nm, respectively. In this case, there is slightly increase in the crystallite size of sample synthesized at pH 9 due to the attachment of the small particles. However, the smallest crystallite size of $In(OH)_3$ NPs is obtained at pH 10 as compared to those synthesized at pH 8, 9 and 11. This can be explained by the high concentration of the solute (supersaturation) at pH 10 resulted in the formation of minimum radius of crystallites (Kohli et al., 2011; Kukushkin & Nemna, 2001).

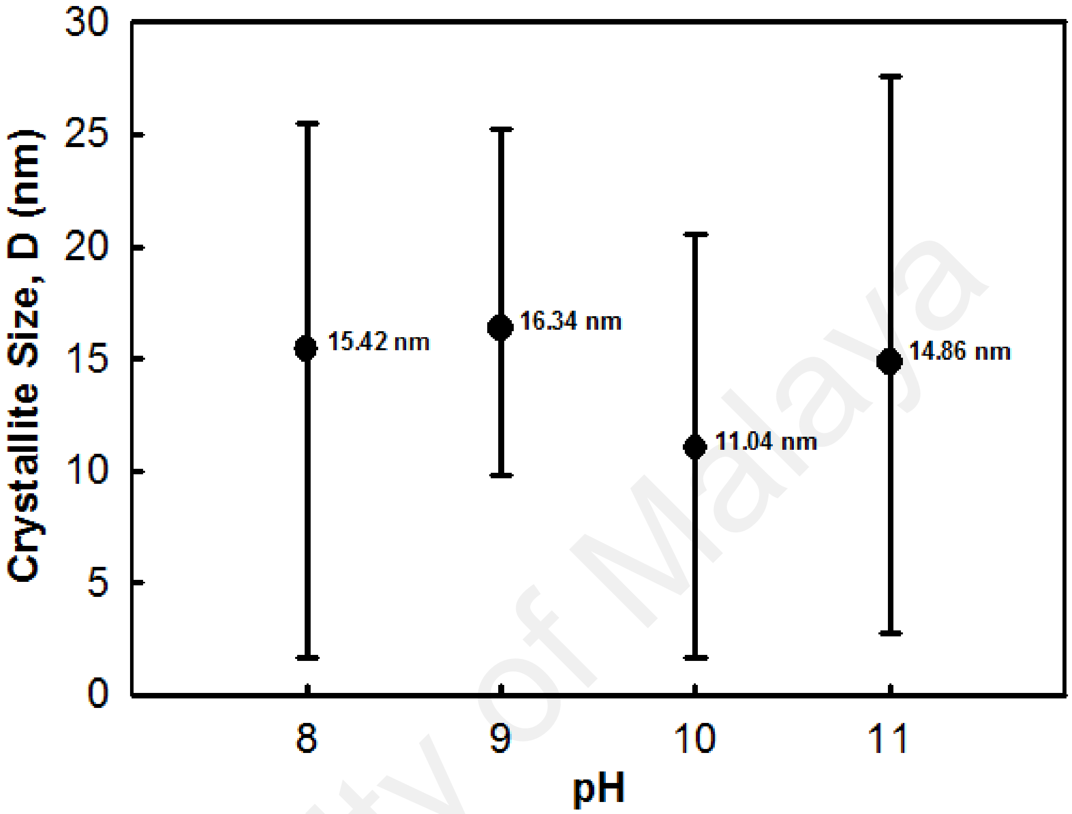

Figure 4.2: Crystallite size of as-synthesized In(OH)$_3$ NPs at different pH values.

Besides that, the crystallite size of In(OH)$_3$ NPs was also calculated by using Williamson-Hall (W-H) models as shown in Eq.(3.6). Figure 4.3 shows the W-H plot analysis for all samples. Strain ($\mathcal{E}$) is the gradient of the graph and $K\lambda/D$ is the intercept of the graph where D can be calculated from the values. In addition, five points with goodness of fit (r^2) of 0.833 - 0.961 are selected from the distribution values.

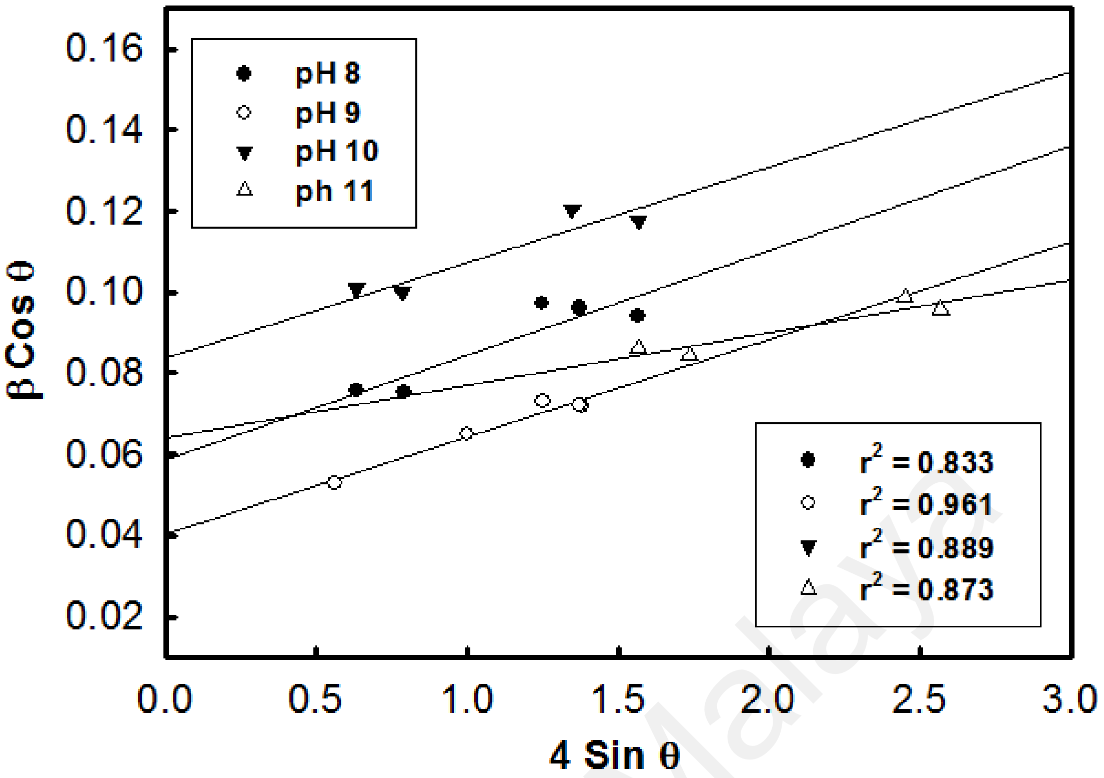

Figure 4.3: W-H plot of as-synthesized $In(OH)_3$ NPs at different 8, 9, 10 and 11 pH values.

Figure 4.4 shows the relationships of crystallite size, strain and pH values where the crystallite size of $In(OH)_3$ NPs was increased from 23.57 to 34.47 nm as the pH value increases from 8 to 9. However, the crystallite size of $In(OH)_3$ NPs decreased significantly to 16.54 nm as the pH value was continually increased to pH 10. The crystallite size of $In(OH)_3$ NPs were further increased to 21.68 nm at pH 11. The microstrain of $In(OH)_3$ NPs for pH values 8, 9, 10 and 11 was 0.0257, 0.0241, 0.0235 and 0.0136, respectively. Hence, the crystallite size for $In(OH)_3$ NPs calculated from Scherrer equation and W-H model was found to be in a similar trend. However, it shows that sample pH 10 has the smallest crystallite size for both calculations.

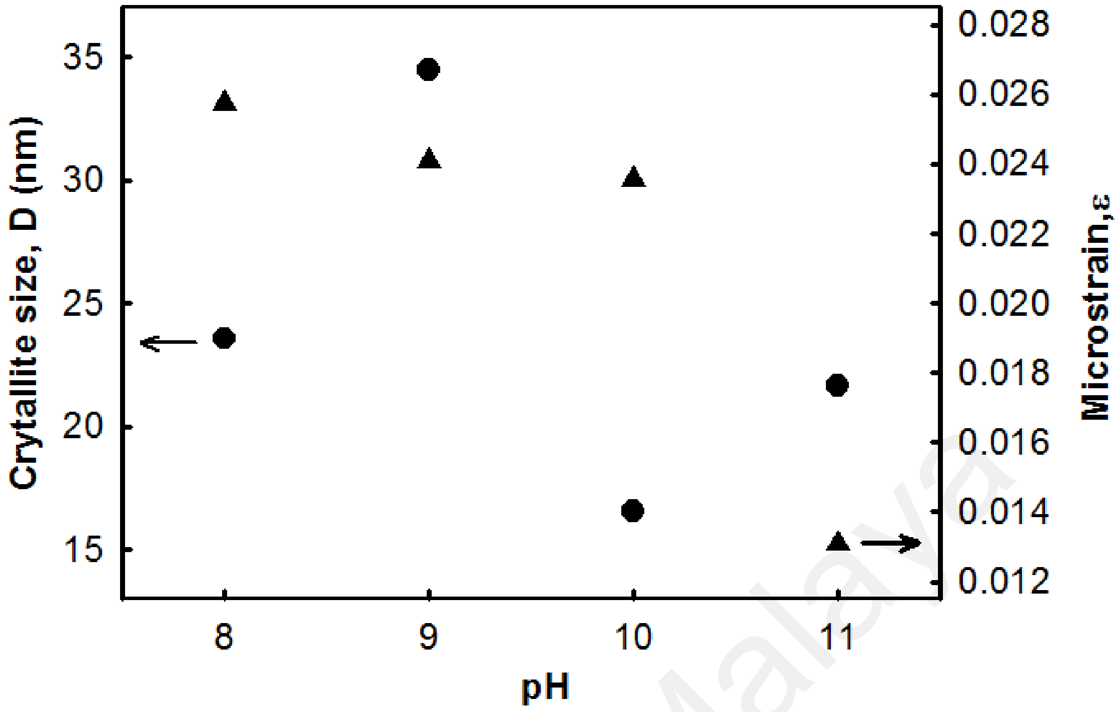

Figure 4.4: Relationship of crystallite size and microstrain as the function of pH values (8, 9, 10 and 11).

4.2.2 FTIR spectroscopy analysis

Figure 4.5 shows the FTIR spectra (500-4000 cm^{-1}) of $In(OH)_3$ NPs studied at different pH values. The adsorption bands located at 3240, 3035 and 1745 cm^{-1} are corresponding to the O-H stretching and bending vibrations of hydroxyl group. This confirmed the existence of crystallization of water molecules (Ayeshamariam et al., 2013; Cao et al., 2010; Wan et al., 2015; Zhu et al., 2005). The peaks located at 1160, 1034, 821, 777 and 708 cm^{-1} represent to the In-OH bonds of $In(OH)_3$ assigned as in-plane deformation and liberation mode of vibrations of hydroxyl groups (Cao et al., 2010; Selvakumar et al., 2014; Tseng & Tseng, 2009). In addition, the peaks at 487 cm^{-1} which were detected can be attributed to In–O vibrations of In–OH (Selvakumar et al., 2014). The 1417 and 1300 cm^{-1} modes are detected as C-O stretching vibration modes represent the presence of ethanol. However, the C-O bands are appeared because the combination of indium ions (In^{3+}) with the ethanol unit produces a longer chain and further self-assemble to form a ordered shape via van der Waals interactions (Gao et al., 2015; Xu & Wang, 2009).

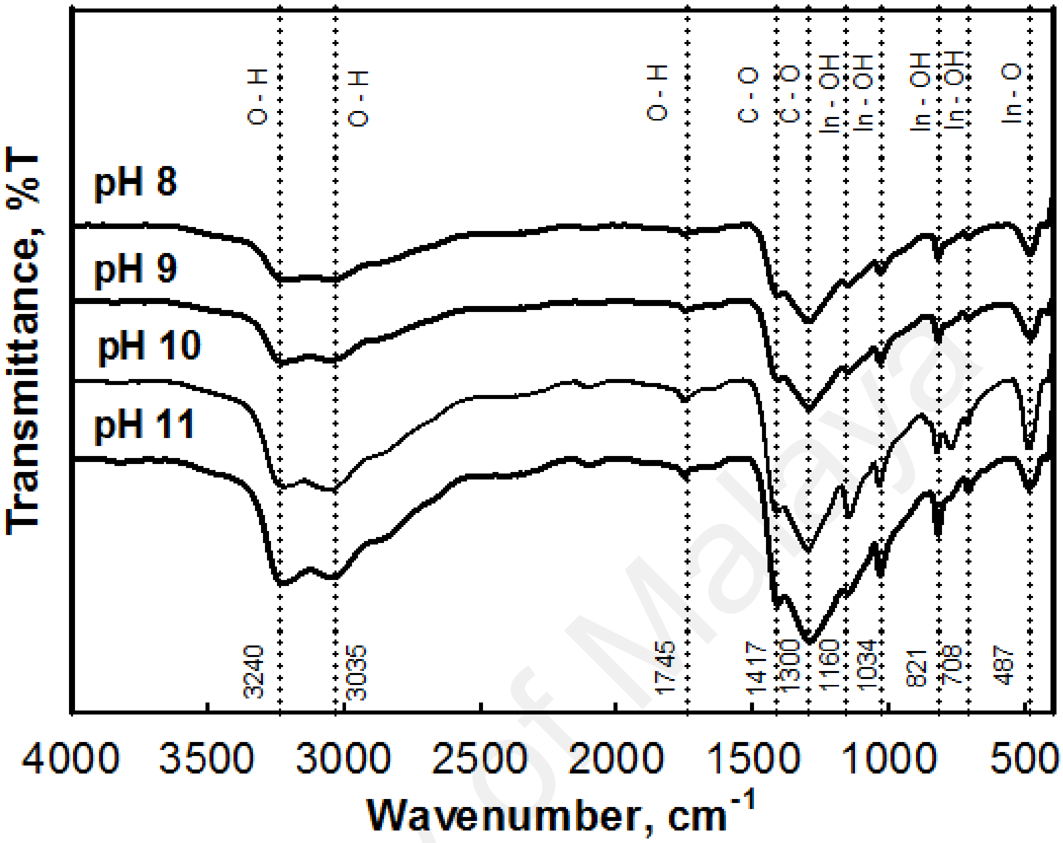

Figure 4.5: FTIR spectra of as-synthesized In(OH)$_3$ NPs at different pH values (8, 9, 10 and 11).

It is observed that the peaks at 3240, 3035, 1417, 1300, 1034, 821 and 708 cm^{-1} become sharper as the pH gradually increased from 8 to 11. Moreover, the intensities of the observed peaks located at 1745, 1160 and 487 cm^{-1} increase as the pH increased from 8 to 10, but apparently reduced even through the pH was further increased to 11.

4.2.3 Raman spectroscopy analysis

Furthermore, the structure properties of In(OH)$_3$ NPs were investigated by Raman spectroscopy as shown in Figure 4.6. The entire Raman shift peaks at 309 and 484 cm^{-1} are assigned to the phonon vibration modes of cubic In(OH)$_3$ (Motta et al., 2010; Wan et al., 2015). It shows that intensity peak is increased from pH 8 to 11 at 309 cm^{-1}. Besides that, it was observed that the peak intensities of 484 cm^{-1} gradually decrease at pH values 8 to 9 and slightly increase when the pH values reached 11. The highest peak intensity occurred at sample of pH 11 due to larger range of crystallite size distribution (Scherrer analysis). Rani et.al (2008) stated that when the pH values are above 9, the particles size tends to decrease due to dissolution of nanoparticles. However, in this case, the particles size is slightly increased as pH values increase from pH 10 to 11. Thus, no dissolution of nanoparticles is occurred as the pH higher than 10 in this case. Smaller nanoparticles are agglomerated to become larger particles (Chithra et al., 2015).

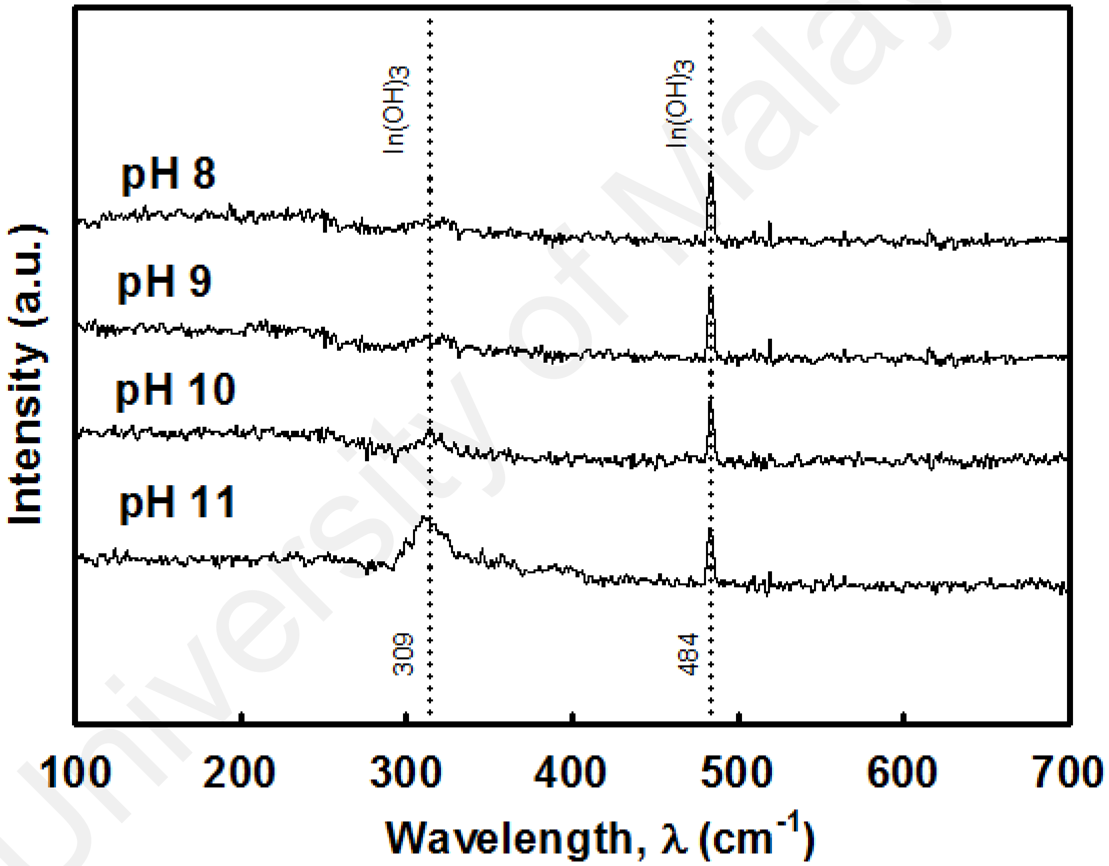

Figure 4.6: Raman spectra of as-synthesized In(OH)$_3$ NPs at different 8, 9, 10 and 11 pH values.

4.2.4 HRTEM analysis

Figure 4.7 (a-d) shows the HRTEM images of the In(OH)$_3$ NPs synthesized at 8, 9, 10 and 11 pH values. It can be observed that the In(OH)$_3$ NPs are in the cubic shape.

In this figure, the dark region represents the agglomeration of the small particles where the large particle is formed. However, the average particles sizes of $In(OH)_3$ NPs are 14.28, 20.59, 11.76 and 17.64 nm at pH values 8, 9, 10 and 11, respectively. The particles size distribution appears less homogeneous as shown in Figure7a and b, whereas it appears better homogeneous as shown in Figure 7c and d. High surface area of nanoparticles tends to agglomerate due to Van der Waals interaction (Man et al., 2014). HRTEM analysis reveals that the smallest particle size is obtained at pH 10. When the pH is low, nucleation of nanoparticles does not proceed well since there is lack of OH^- ions in the solution. Therefore, new nuclei formed in the solution are unstable leading to grow into larger particles. The largest nanoparticle was observed in the present work when $In(OH)_3$ NPs are synthesized at pH 9 (20.59 nm). However, at an optimum pH value (pH 10) where OH^- ions increase, a large number of nuclei are formed which minimizes the radius of crystallite size. Hence, smallest particles size is formed at pH 10 (11.76 nm). As pH is further increase to 11, the small particles were attached to each other into larger particles (Chithra et al., 2015). This inference can be supported by XRD, FTIR and Raman analysis showing that the peak intensity is higher at pH 11.

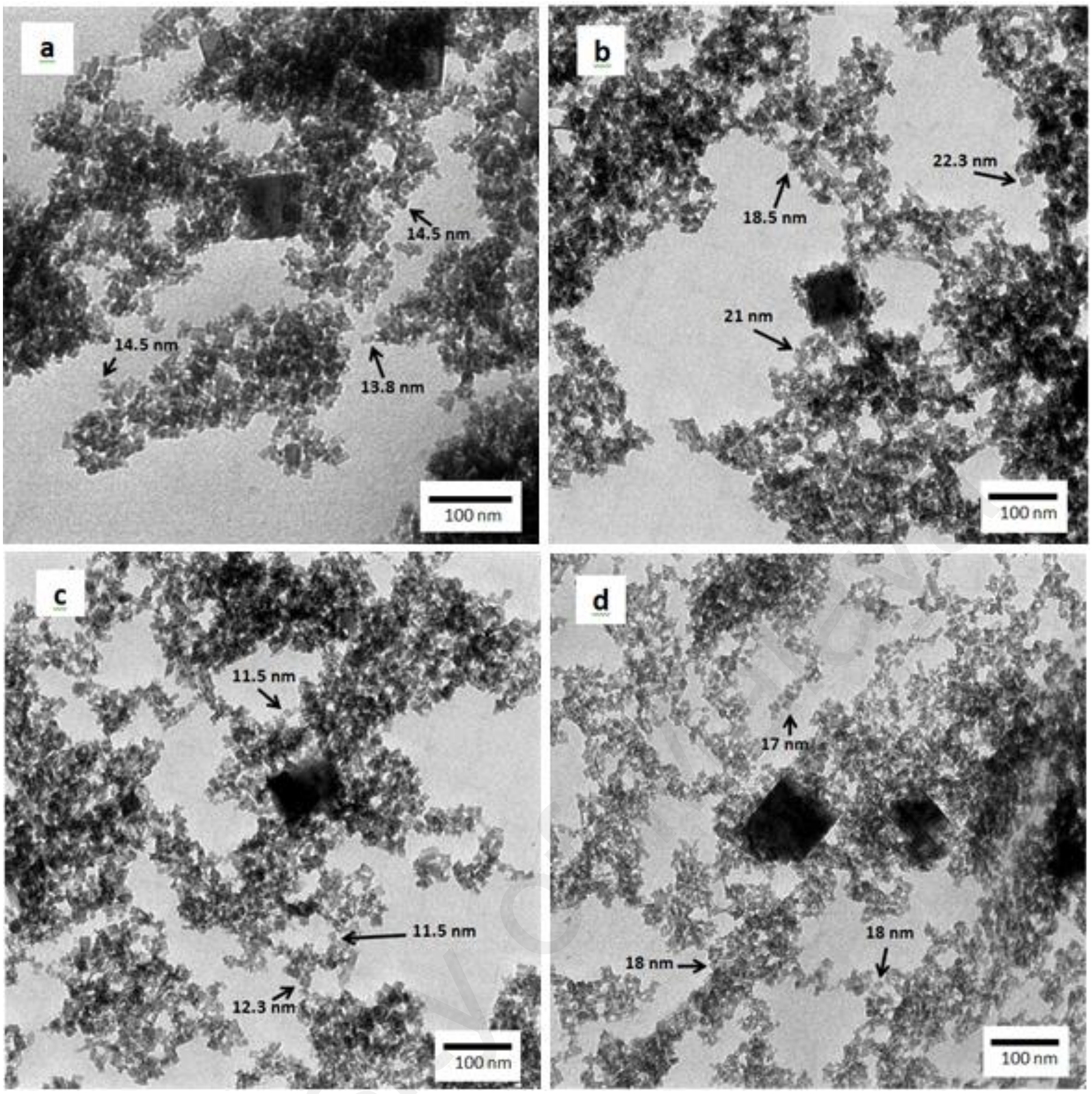

Figure 4.7: TEM images of $In(OH)_3$ NPs synthesized at different pH values (a) 8 (b) 9 (c) 10 and (d) 11.

4.2.5 Zeta potential measurement

The change of zeta potential (ξ) and particle size distribution are shown in Figure 4.8. It can be seen that the absolute value of zeta potential of the $In(OH)_3$ NPs synthesized at pH 8 and 9 occurred near to the isoelectric point (IEP) at -0.128 and -1.60 mV. This is the point where the highest agglomeration of particles occurred. Here, the particles aggregate up to 139 and 144 nm in size. However, the maximum positive net charges of 3.68 mV associated with smallest size distribution of 92.6 nm are found when further increased to pH 10 and sample pH 11 has -2.45 mV with 137.9 nm in size. Thus, it can be concluded that $In(OH)_3$ NPs synthesized at pH 10 have the maximum stability within pH range of 8-11.

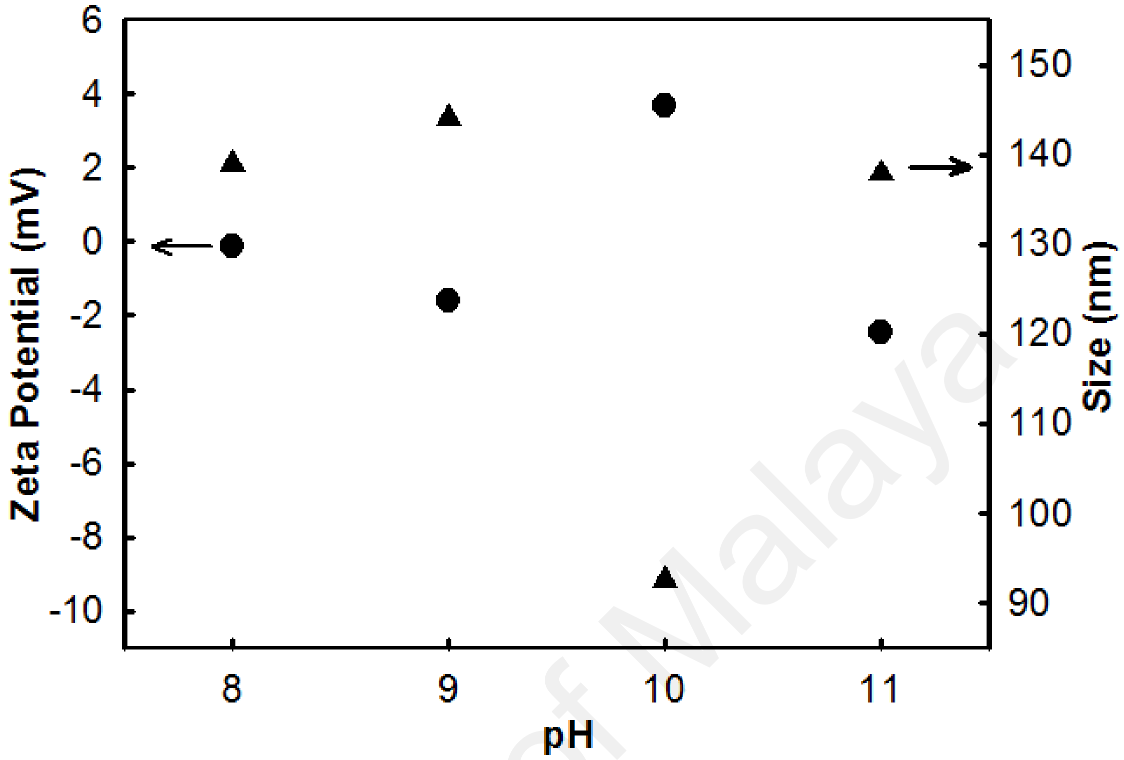

Figure 4.8: Zeta potential and particle size distribution of $In(OH)_3$ NPs as the function of different pH values (8, 9, 10 and 11).

4.2.6 Nucleation and growth mechanism of $In(OH)_3$ NPs

$In(OH)_3$ NPs were synthesized at different pH values (8,9,10 and 11) using co-precipitation method in the present work since there is no report on the structure properties of $In(OH)_3$ NPs with higher pH values ranging from 8 to 11 over the past decades. Recently, Amirsalari et al. (2015) reported that alumina (Al_2O_3) nanoparticles were prepared at pH values (7 to 10) by co-precipitation method. They were found that the optimized nanoparticles were belongs to pH 9. Kohli et al. (2011) showed that synthesized chromium oxide (Cr_2O_3) nanoparticles prepared at pH 9 by co-precipitation route have the smallest nanoparticles size (20.5 nm) as compared to pH 8, 10 and 11. The pH is an important parameter affects the structure properties of the nanoparticles in wet chemical method. Thus, understanding the nucleation and growth mechanism is necessary to make a better control on the structure properties $In(OH)_3$ NPs. In our work, the crystal nucleation and crystal growth of $In(OH)_3$ NPs are controlled by the OH^- concentration in the precursor solution. As we know that a new phase will be formed when the concentration of solute in a solvent exceeds its equilibrium solubility (Thanh et al., 2014). However, there will be no nucleation existed initially after the concentration of the solute increases above the equilibrium concentration. Nucleation is only occurred when the concentration of growth species reached minimum saturation above the solubility where the solution becomes supersaturated. This may lead to increase in nucleation rate of NPs. Hence, the concentration of the growth species will decrease after the initial nucleation where no nuclei will form and subsequent growth until the concentration of growth species reached the equilibrium concentration. Once nuclei are formed, growth will proceed simultaneously (Thanh et al., 2014).

Figure 4.9 shows the structure of $In(OH)_3$ NPs in the precursor solution. The formation of $In(OH)_3$ NPs is divided into few steps that are hydrolysis, condensation and polymerization of monomers and particles growth. In order to form a highly crystallite of $In(OH)_3$ NPs, the sufficient amount of OH^- ions in the precursor solution is necessary. In this case, the zero charge of precursor molecules $In(NO_3)_2.9H_2O$ is necessary to be formed by reacting with a sufficient water to allow condensation.

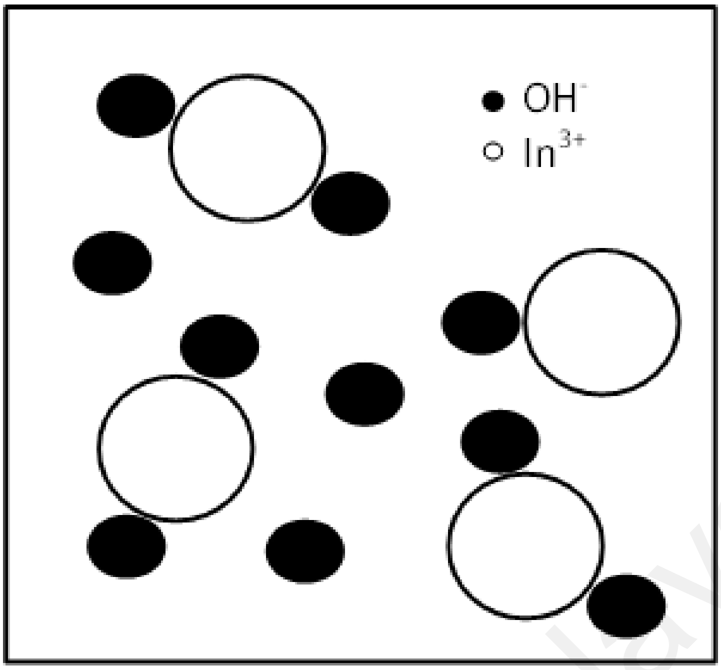

Figure 4.9: Schematic representation of the structure of $In(OH)_3$ NPs during synthesis process.

In the initial stage, no precipitate was observed when the aqueous solution of $In(NO_3)_2.9H_2O$ was reacted with distilled water. However, white precipitate was observed after the ammonium hydroxide (NH_4OH) was added into the solution. NH_4OH was continuously added until the solution turns to the desired pH values. Formation of $In(OH)_3$ NPs can be described by the following chemical reaction:

$$In(NO_3)_2.9H_2O + NH_4OH \rightarrow In(OH)_3 + N_2H_4O_3 + H_2O \qquad (4.1)$$

As the pH increases from 8 to 11, the nucleation process is continuous until the solution became supersaturated. High concentration of OH^- ions in the solution will cause $In(OH)_3$ NPs to react back with OH^- ions. Hence, the dissolution of $In(OH)_3$ NPs is occurred leading to formation of smaller particles and they become agglomerated as shown in Figure 4.10 (Alias et al., 2010; Wahab et al., 2009).

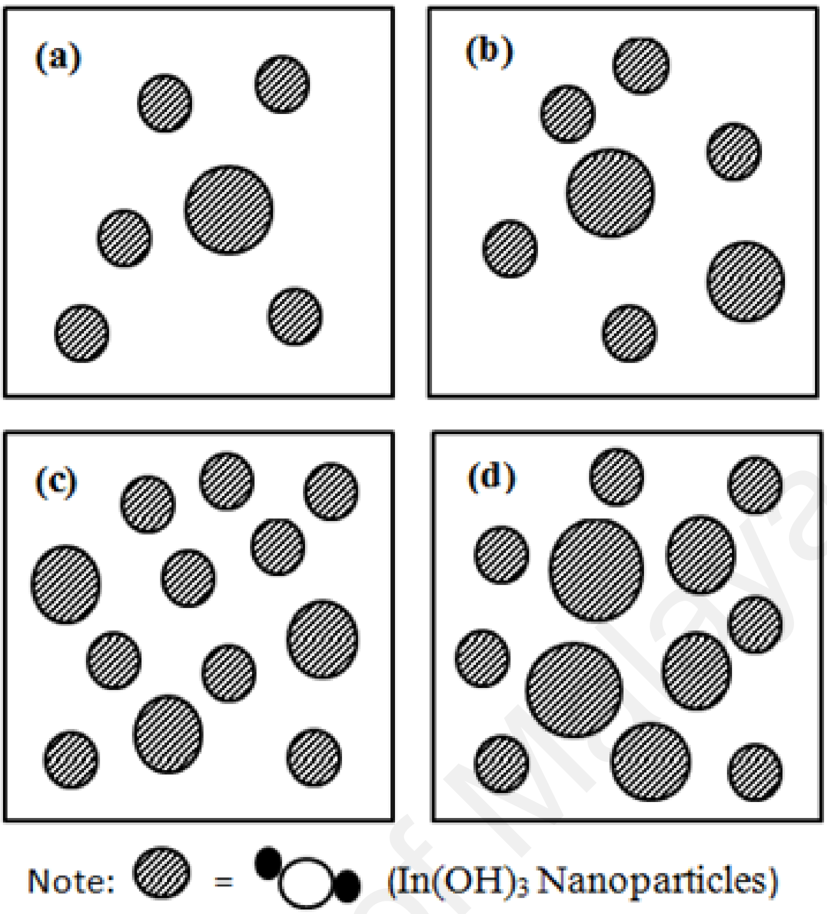

Figure 4.10: Schematic representation of the distribution and different size of In(OH)$_3$ NPs at different pH values: (a) 8; (b) 9; (c) 10 and (d) 11.

The morphology and crystal size of the products are depending on the reaction rate of crystal nucleation or crystal growth since the OH$^-$ concentration increased with pH values increased. The competition between crystal nucleation and crystal growth of nanoparticles are determined by the inherent crystal structure and the chemical potential of the precursor solution. A small crystal size of In(OH)$_3$ NPs will be formed with low aspect ratio if the nucleation rate is faster than crystal growth. Inversely, fast crystal growth rate contributed to the large crystal size and high aspect ratio of the crystal along preferential directions (Hu et al., 2009; Kam et al., 2004). On the other hand, the surface tension between the OH$^-$ ions and the precipitate In(OH)$_3$ NPs is an important parameter in the nucleation process (Sohnel, 1982). Formation of new phase leads to increase in surface energy and decrease in free energy of solution according to classical homogeneous nucleation theory. The decreasing free energy becomes the driving force of the formation new phase. The nucleation rate (J) of the $In(OH)_3$ NPs was calculated in the form of Arrhenius reaction velocity equation according to the classical nucleation theory as shown in Eq. (4.2) (Ruiz-Agudo et al., 2015; Thanh et al., 2014).

$$J = A\exp\left[-\frac{\beta E_s{}^2 V_m{}^3}{v^2 (k_B T)^3 (InS)^2}\right] \tag{4.2}$$

where A is the pre-exponential factor; E_s is the interfacial energy; β is the geometrical parameter about the crystal shape (16π/3 for spherical nucleus); V_m is the molar volume of crystal; v is the ion number; k_b is the Boltzmann constant (1.3805×10^{-23} J/K); T is the absolute temperature (K) and S is the supersaturation of solution. The nucleation rate of $In(OH)_3$ NPs for pH values of 8,9,10 and 11 was 1.16, 1.29, 1.39, and. 1.57 $m^5J^{-1}mol^{-1}$. It was confirmed that the nucleation of $In(OH)_3$ NPs was increased gradually when the pH values increased. However, in our work, the size of $In(OH)_3$ NPs does not decrease with increasing pH values from 8 to 11. This is because the chance of attraction between small $In(OH)_3$ NPs increases due to Ostwald ripening and aggregation since larger number of small $In(OH)_3$ NPs were formed at higher pH values in the nucleation process. The larger $In(OH)_3$ NPs will be formed.

The OH^- concentration is not only acted as the nucleation agent but also as a surfactant in the wet chemical method (Hu et al., 2009). The balance between the chemical potential and the rate of ionic motion in the precursor solution is strongly affected by the pH values. In addition, the transport and behavior of $In(OH)_3$ NPs in the aquatic environment are determined by their intrinsic properties in terms of the stability and surface energy of NPs in the presence of OH^- concentration. These $In(OH)_3$ NPs will become mobile and distributed depend on their dissolution and disaggregation behavior as a result of interactions with the surrounding environment (OH^- ions). Based on the theory, repulsive force of NPs is developed when the distance between the surfaces of two particles is larger than the combined thickness of the electrical double layers of two particles and there is no overlap of the diffusion double layer. When the NPs attached to each other, two double layers can be overlap and aggregated (Mudunkotuwa & Grassian, 2010; Pettibone et al., 2008). pH is one of the abiotic factors that strongly influence the transport and mobility of the NPs in the subsurface, in particular, when the NPs are in a stable dispersion rate. The NPs become destabilizes and aggregate easily when they are close to the pH_{PZC} (Guzman et al., 2006; Palomino & Stoll, 2013). Thus, stable $In(OH)_3$ NPs will be formed when the pH values of the solution are far from the pH_{PZC} of NPs which NPs discharge themselves in high OH^- concentration solution.

4.3 Calcination temperatures effects

Based on the earlier investigation on the effect of pH variation on the stability and structural properties of the $In(OH)_3$ NPs synthesized by co-precipitation method, it has been examined that $In(OH)_3$ NPs synthesized at pH 10 was the optimum parameter, as it gave the smallest particles size (11.76 nm) and maximum stability (3.68 mV). In this experiment, the pH value was fixed at 10 and the calcination temperatures function as variable. The $In(OH)_3$ NPs were synthesized at an optimum pH 10 by co-precipitation method and calcined at 200, 300, 400, 500 and 600 ℃, respectively.

4.3.1 Thermogravimetric (TGA and DTA) analysis

In the present work, as-prepared $In(OH)_3$ NPs were oxidized to In_2O_3 NPs by calcination. Before the calcination process was conducted, the thermal decomposition behaviour of as-prepared $In(OH)_3$ NPs were investigated via TGA and DTA in the temperature range of 25 to 1000 ^oC. Meanwhile, the transition temperature of as-prepared $In(OH)_3$ NPs were determined. Figure 4.11 shows the typical DTA and TGA curves of the as-prepared $In(OH)_3$ NPs synthesized via co-precipitation method. From the TGA analysis curves, it was observed that an initial weight loss of the as-prepared $In(OH)_3$ NPs were take place at about 10% up to around 200 ^{o}C. This is because the desorption of the absorbed water molecules of as-prepared $In(OH)_3$ NPs (Liu et al., 2008; Selvakumar et al., 2014; Tseng & Tseng, 2009). Besides, it can be seen that there was a second weight loss of as-prepared $In(OH)_3$ NPs occurred from 200 to 300 ^{o}C at about 40%. The second weight loss was ascribed as the co-condensation reaction among the hydroxyl groups during dehydration of the as-prepared $In(OH)_3$ NPs led to the formation of In_2O_3 NPs. From here, it was considered that the In_2O_3 NPs might start to form above 300 ^{o}C since most of the weight loss was observed in which related to the following reaction (Tseng & Tseng, 2009; Yang et al., 2004; Zhan et al., 2004):

$$2In(OH)_3 \rightarrow In_2O_3 + 3H_2O \tag{4.3}$$

Furthermore, the weight loss of as-prepared $In(OH)_3$ NPs occurred between the 300 and 600 ^{o}C was associated with the decomposition of the trapped surfactant molecules which surrounded the as-prepared $In(OH)_3$ NPs (Selvakumar et al., 2014). There was no obvious weight loss observed above 600 ^{o}C.

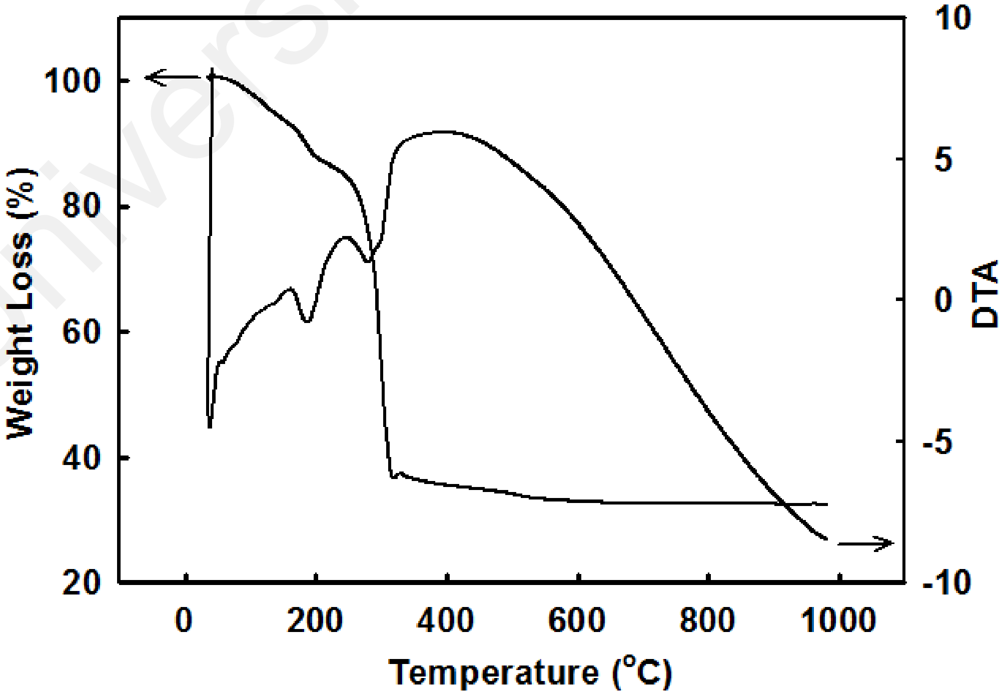

Figure 4.11: TGA and DTA curves of the as-prepared $In(OH)_3$ NPs synthesized at pH 10 via co-precipitation method.

Correspondingly, DTA analysis as-prepared In(OH)$_3$ NPs was conducted and recorded in the similar temperature range of TGA analysis in order to determine its decomposition steps. DTA curve of as-prepared In(OH)$_3$ NPs revealed that two broad endothermic peaks were located at around 180 and 280 ^{o}C and an exothermic peak located at 390 ^{o}C. These broad endothermic peaks at 180 and 280 ^{o}C were assigned to the physical evaporation of water molecules from samples and de-bonding reaction of the terminal and bridging hydroxyl groups of In(OH)$_3$ NPs, respectively (Parast & Morsali, 2011; Pramanik et al., 2002). The exothermic peak at 390 ^{o}C was found due to the evaporation of the trapped surfactant molecules where most probably ascribed to the formation of In$_2$O$_3$ NPs (Motta et al., 2010; Selvakumar et al., 2014). The DTA results served as a well complement to that of the results reflected in TGA curves. Thus, it showed that the as-prepared In(OH)$_3$ NPs were decomposed completely to form In$_2$O$_3$ NPs when the temperature achieved 300 ^{o}C. This similar phenomena is in well agreement with the results reported by Seetha and Tseng (2009).

4.3.2 X-Ray Diffraction (XRD) Analysis

Figure 4.12 shows the typical XRD patterns of both as-prepared In(OH)$_3$ NPs and calcined In$_2$O$_3$ NPs (200, 300, 400, 500 and 600 ℃) synthesized at pH 10 via co-precipitation method. Figure 4.12(a) represented the XRD patterns of as-prepared In(OH)$_3$ NPs which well-matched to the Inorganic Crystal Structure Database (ICSD) with reference code 01-076-1463 as demonstrated in our previous work (Goh et al., 2016). The diffraction peaks are reflects the formation of body centered cubic (bcc) phase of In(OH)$_3$ NPs synthesized at pH 10. Meanwhile, from Figure 4.12(b-f), it was observed that the XRD patterns of calcined In$_2$O$_3$ NPs are strictly matched to the Inorganic Crystal Structure Database (ICSD) with reference code 01-071-2194. The calcined In$_2$O$_3$ NPs were present at angles of 2θ = 30.88°, 35.71°, 51.30°, 60.76°, 83.37° and 85.84° with well oriented along the (222), (420), (440), (622), (662), and (048) directions, respectively. All diffraction peaks of calcined In_2O_3 NPs were ascribed to the cubic structure with lattice constant, a = 10.1170 Å. Thereby, it was indicated that original morphology of the $In(OH)_3$ NPs was kept after calcination. Moreover, the peak intensity of In_2O_3 NPs was increased with the increasing of calcination temperature from 200 to 600 ℃. This can be explained by its better crystallinity of In_2O_3 NPs at higher temperature (Selvakumar et al., 2014). The short range order of the samples has an inherent tendency to become a long range order which will increase the intensity of XRD pattern (Seetha et al., 2012; Selvakumar et al., 2014). Besides, it was noticed that a few of diffraction peaks of cubic $In(OH)_3$ were detected at 200 ℃. Those presented $In(OH)_3$ peaks indicated that transformation of cubic $In(OH)_3$ NPs to In_2O_3 NPs were not fully achieved. However, $In(OH)_3$ NPs peaks disappeared when the calcination temperature was slightly increased up to 300 ℃. Hence, these obtained results indicated that the conversion of $In(OH)_3$ NPs to In_2O_3 NPs depend on the calcination temperature (Selvakumar et al., 2014).

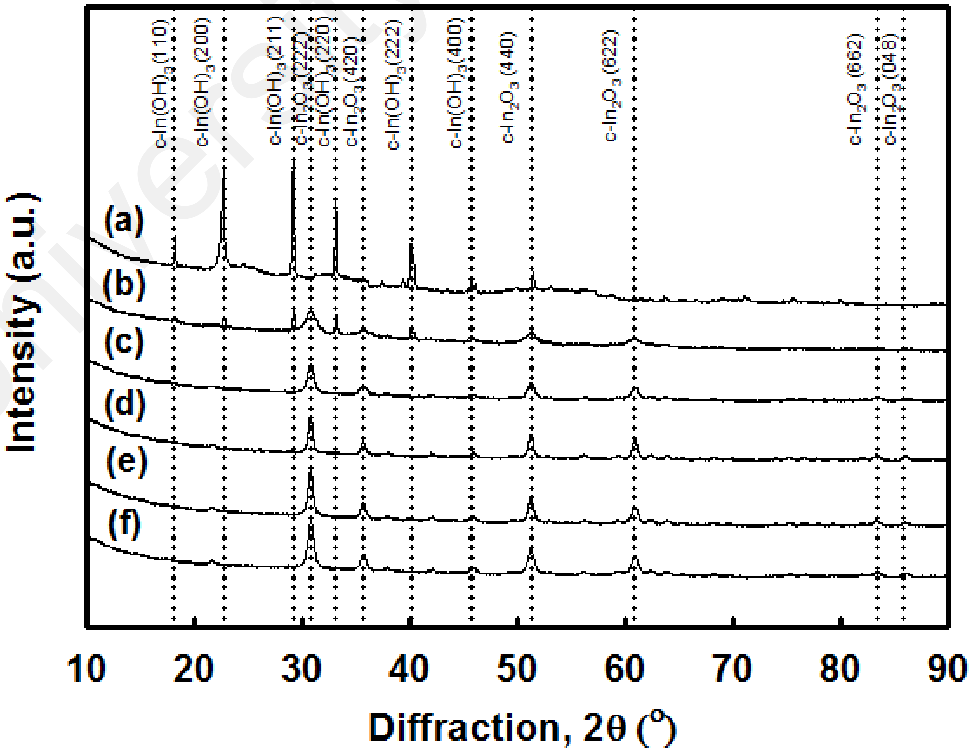

Figure 4.12: XRD patterns of $In(OH)_3$ NPs and In_2O_3 NPs: (a) as-prepared $In(OH)_3$ NPs; (b-f) In_2O_3 NPs calcined at 200 ℃, 300 ℃, 400 ℃, 500 ℃, and 600 ℃, respectively.

The crystallite size of the In_2O_3 NPs was calculated by using Debye-Scherrer equation as shown in Eq.(3.2). The average crystallite size of In_2O_3 NPs was determined by all of the presented diffraction peaks. Figure 4.13 shows the average crystallite size of In_2O_3 NPs for different calcination temperature of 200, 300, 400, 500 and 600 ℃ are 5.16, 3.36, 3.66, 4.57, and 4.90 nm, respectively. Based on the obtained results, a slight decreased in the crystallite size of In_2O_3 NPs at 300 ℃ was observed. This was because of the shrinking of crystallite size when the as-prepared $In(OH)_3$ NPs were completely transferred to In_2O_3 NPs (Guoa et al., 2011). It is well known that the as-prepared $In(OH)_3$ NPs is subjected to decomposition at high temperature where water and other volatile matter are gives off and produces In_2O_3 NPs. However, the crystallite size of In_2O_3 NPs increased in the range of 300 to 600 ℃. This can be explained through the coalesce of NPs with increasing calcination temperature results in the formation of larger crystallite size (Flores-Mendoza et al., 2008; Selvakumar et al., 2014). Similar phenomenon has been reported by Seetha et al. (2012) through the preparation of cubic In_2O_3 at 300, 500 and 700 ℃ by hydrothermal method. They observed that the average crystallite size of cubic In_2O_3 were gradually increased which were 37 nm at 300, 40 nm at 500 and 43 nm at 700 ℃. Forsh et al. (2014) also showed that the size of In_2O_3 NPs synthesized by sol gel method was increased from 8 to 20 nm when the calcination temperature was increased.

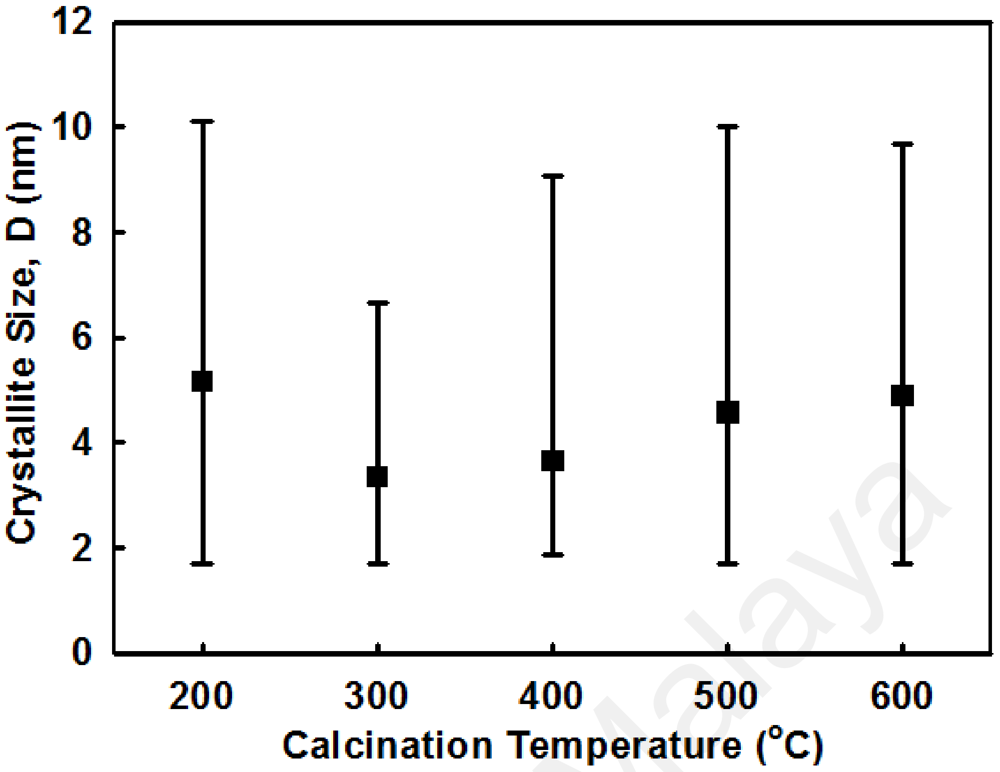

Figure 4.13: Crystallite size of In_2O_3 NPs calcined at different temperatures (200 ℃, 300 ℃, 400 ℃, 500 ℃ and 600 ℃).

Furthermore, the crystallite size of In_2O_3 NPs was also calculated using Williamson-Hall (W-H) models as shown in Eq.(3.6). Figure 4.14 shows the W-H plot analysis for all samples. $K\lambda/D$ is the intercept of the graph where D can be calculated from the values and $\mathcal{E}$ (strain) is the gradient of the graph. Besides, five points with goodness of fit (r^2) of 0.9377 - 0.9962 were selected from the distribution values.

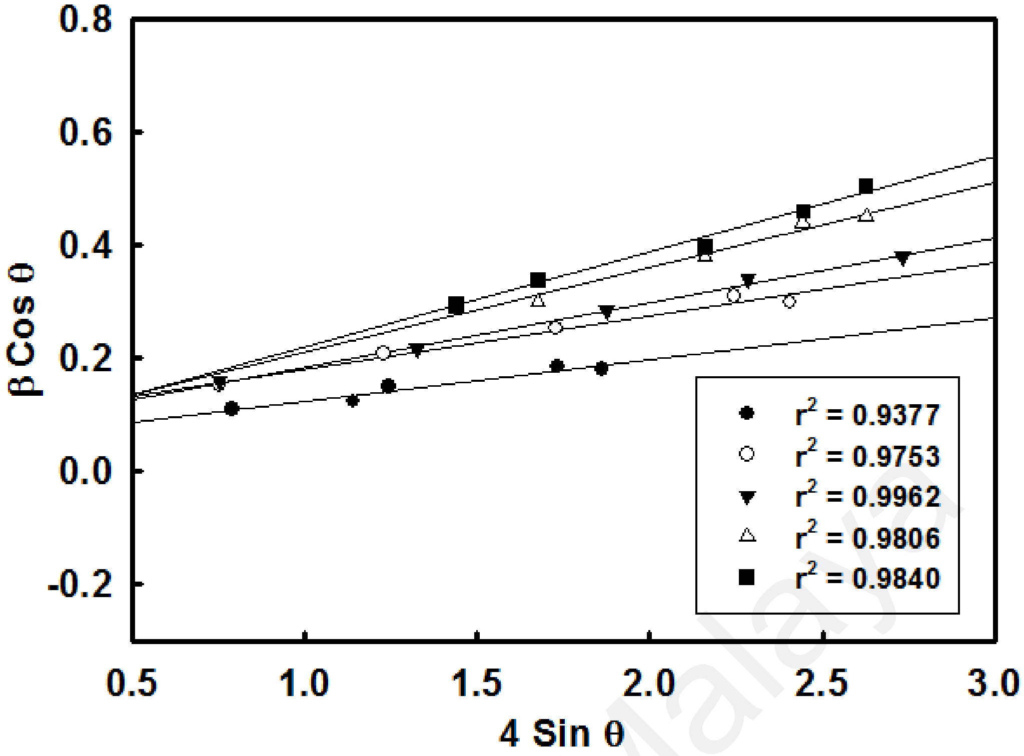

Figure 4.14: W-H plot of In_2O_3 NPs calcined at different calcination temperatures of 200 °C, 300 °C, 400 °C, 500 °C and 600 °C.

Figure 4.15 shows the relationships of crystallite size, strain and calcination temperature where the crystallite size of In_2O_3 NPs were decreased from 27.79 nm to 16.03 nm as the calcination temperature increases from 200 to 300 °C. Somehow, crystallite size of In_2O_3 NPs increased slightly to 19.58, 22.66 and 27.19 nm as the calcination temperature was continually increased to 400, 500 and 600°C, respectively. Furthermore, the microstrain of In_2O_3 NPs for different calcination temperature (200, 300, 400, 500 and 600 °C) was 0.0736, 0.0944, 0.1144, 0.1500 and 0.1647, respectively. Therefore, a similar trend was found in crystallite size of In_2O_3 NPs after calculated from both Scherrer and W-H equation. This fact conveys that the higher temperature of 300 °C applied to In_2O_3 NPs has the smallest crystallite size for both calculations.

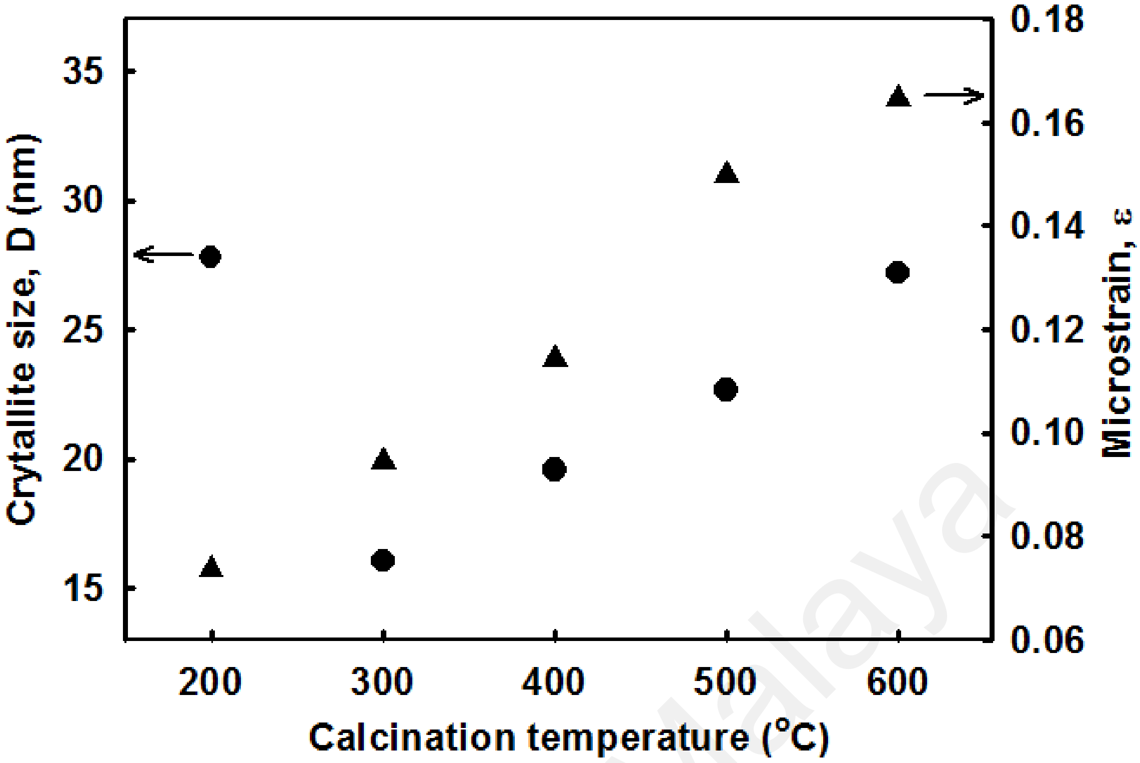

Figure 4.15: Relationship of crystallite size and microstrain of In_2O_3 NPs as the function of calcination temperatures (200 ℃, 300 ℃, 400 ℃, 500 ℃ and 600 ℃).

4.3.3 FTIR spectroscopy analysis

Figure 4.16 shows the FTIR spectra (500-4000 cm^{-1}) of In_2O_3 NPs recorded at different calcination temperatures. In these spectra, the adsorption bands observed at 3240, 3035 and 1684 cm^{-1} were characteristic of bending vibrations and O-H stretching mode of hydroxyl (-OH) group represents the presence of crystallization of water molecules (Ayeshamariam et al., 2013; Cao et al., 2010; Wan et al., 2015; Zhu et al., 2005). The adsorption peak observed at 1562 cm^{-1} mode was assigned as C-O stretching vibration mode indicated the present of ethanol. The appearance of C-O band was due to the association of the ethanol unit with indium ions (In^{3+}) to produce a longer chain and facilitate self-assemble to become an ordered shape through van der Waals interactions (Gao et al., 2015; Xu & Wang, 2009). Other peaks located at 1405, 1039, 831, and 719 cm^{-1} were corresponding to the In-OH bonds of $In(OH)_3$ ascribed to liberation mode of vibrations and in-plane deformation of hydroxyl groups (Cao et al., 2010; Selvakumar et al., 2014; Tseng & Tseng, 2009). Furthermore, detected peaks at 598, 562 and 450 cm^{-1} can be assigned to In–O vibrations phonon of In–OH and were characteristic of the cubic In_2O_3 (Selvakumar et al., 2014; Singh & Mehta, 2003).

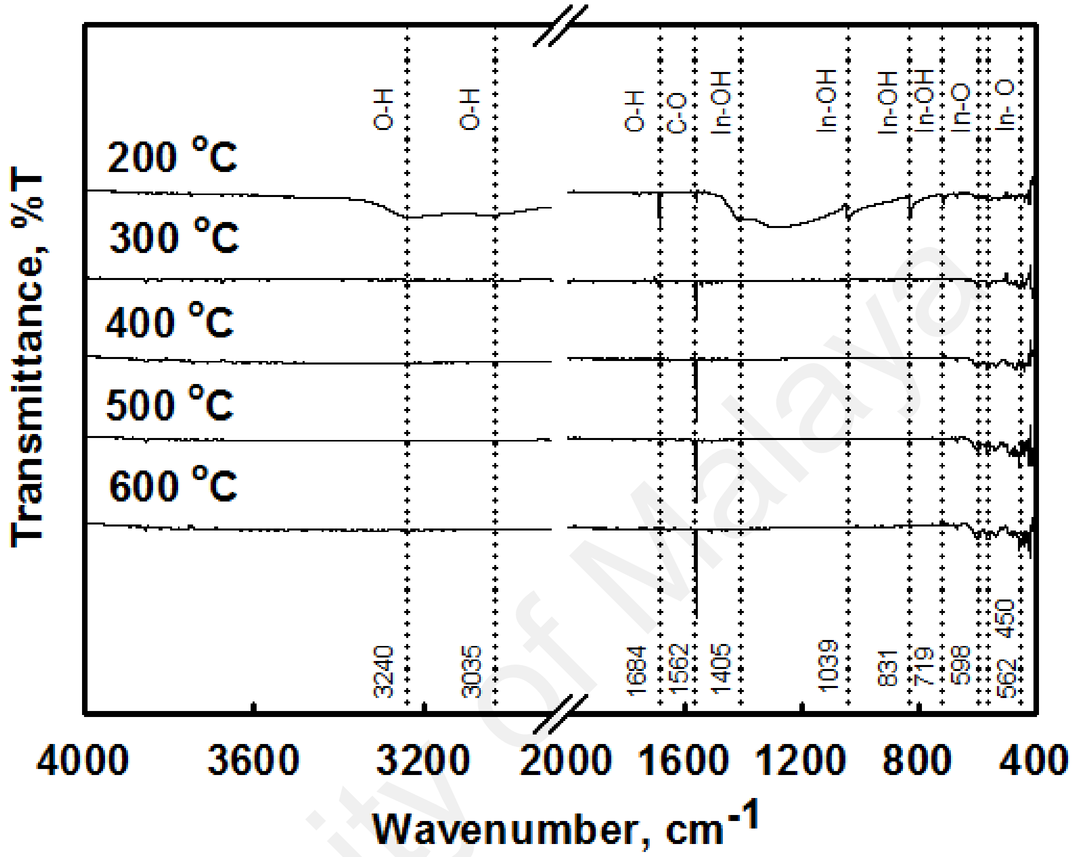

Figure 4.16: FTIR spectra of In_2O_3 NPs calcined at different temperatures (200 °C, 300 °C, 400 °C, 500 °C and 600 °C).

It was observed that the peaks at 1562 cm^{-1} were become sharper when the calcination temperatures increased from 200 to 600°C. Besides, the peak located at 3240, 3035, 1684, 1405, 1039, 831 and 719 cm^{-1} didn't exhibit any infrared features of the hydroxyl groups upon further calcined at 300 °C and beyond. This shows that the loss of water in the samples occurred during calcination process. Furthermore, it can be observed that the absorption peaks of In_2O_3 become more intense and distinct reflects the complete conversion of $In(OH)_3$ to In_2O_3 at 562, 598 and 450 cm^{-1}.

4.3.4 Raman spectroscopy analysis

Figure 4.17 shows the chemical structure of In_2O_3 NPs characterized by Raman spectroscopy in the 100-700 regions over the temperature range from 200 to 600 ℃. The observed Raman shift peaks at 135, 313 and 483 cm^{-1} are ascribed to typical phonon vibrational modes of bcc-structure of In_2O_3 which is matched with those values reported in the literatures (Berengue et al., 2010; Guoa et al., 2011; Hafeezullah et al., 2014; Seetha et al., 2012). The peak at 135 cm^{-1} was attributed to the In-O vibration mode of InO_6 structure units (Yin et al., 2009). The peak at 313 cm^{-1} was correspond to the bending vibration of $\delta(InO_6)$ octahedrons while peak at 483 cm^{-1} can be ascribed to the stretching vibrations of the same $v(InO_6)$ octahedrons (Elouali et al., 2012; Patel et al., 2014).

The bcc-structure $In(OH)_3$ spectrum at 145 and 175 cm^{-1} were observed at 200℃ (Yang et al., 2010). Thus, it revealed that the bcc-In_2O_3 was not completely formed over the temperature until 200℃. However, the intensity of these bands was not existed at temperature of 300 ℃ and above as displayed in Figure 4.17. Furthermore, Raman results show that prominent intensity peaks of bcc-In_2O_3 slightly increased when the temperature was increased from 300 to 600℃. These observations evidence that the improvement of crystallinity of bcc-In_2O_3 NPs (Amirsalari & Shayesteh, 2015; Reddy et al., 2015). Thereby, it indicated that higher calcination temperatures will enhance the crystallite growth of In_2O_3 NPs (Chen et al., 2010).

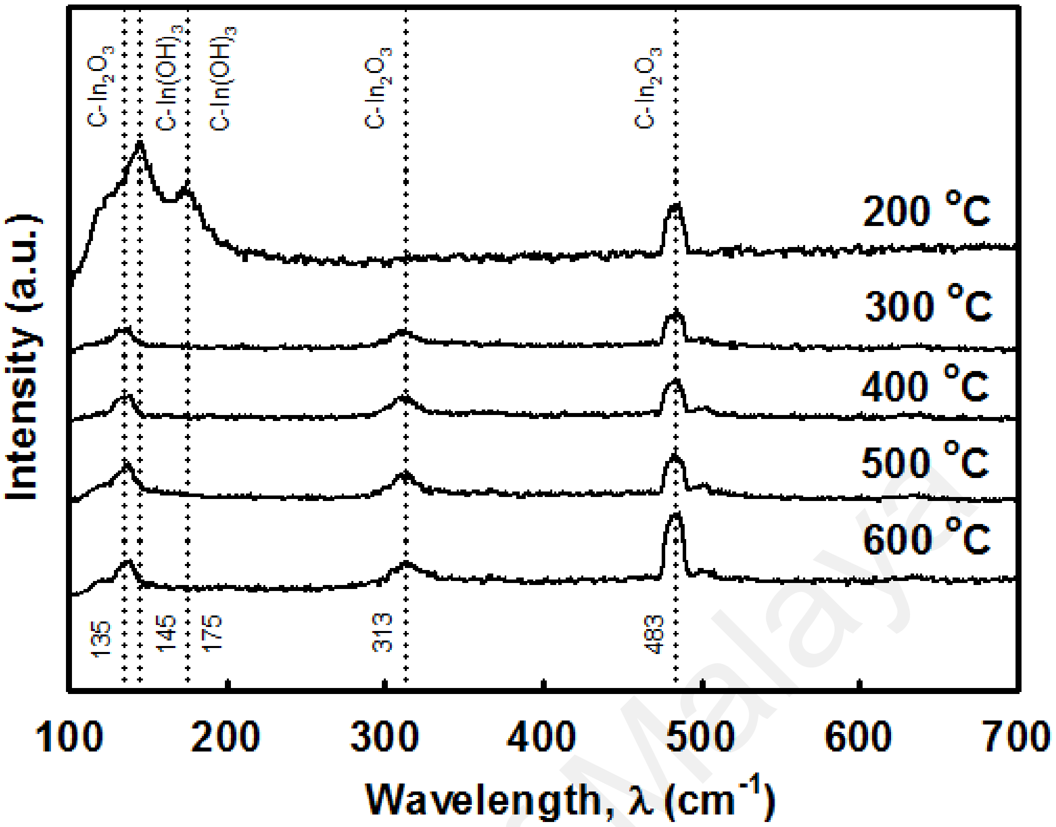

Figure 4.17: Raman spectra of In_2O_3 NPs calcined at different calcination temperatures of 200 °C, 300 °C, 400 °C, 500 °C and 600 °C.

4.3.5 HRTEM analysis

Figure 4.18 (a-j) shows the HRTEM images of the In_2O_3 NPs calcined at 200, 300, 400, 500 and 600 °C. As it can be seen from HRTEM analysis, In_2O_3 powders consisted of NPs and were formed in the round cubic shape. The dark area shows the attraction of the small particles where the larger particles are formed. Besides, the average sizes of In_2O_3 NPs under different calcination temperature of 200, 300, 400, 500 and 600 °C were 18.67, 14.67, 17.67, 20.33 and 27.67 nm, respectively. Here, the particles size In_2O_3 NPs decreased with increasing the calcination temperature from 200 to 300 °C. This is due to completely conversion of $In(OH)_3$ NPs to In_2O_3 NPs occurred at 300 °C which is well agreed with thermogravimetric analysis. The particle size of In_2O_3 NPs becoming smaller as the water molecules in the samples was decomposed. Several researchers reported that In_2O_3 NPs synthesized at a higher calcination temperature above 300 °C via aqueous phase method (Li et al., 2006; Selvakumar et al., 2014; Xiao et al., 2016; Yang et al., 2010). For examples, Selvakumar et al. (2014) reported that the particles size of In_2O_3 NPs about 35 nm were produced after calcined at 400 ℃ prepared by hydrothermal method. Xiao et al. (2016) also showed that the as-prepared $In(OH)_3$ NPs were completely convert into 20 nm of In_2O_3 NPs after calcined at 500 ℃ via solvothermal method.

On the other hand, Niederberger et al. (2006) revealed that In_2O_3 NPs of 5-15 nm were produced by mixing indium (III) acetylacetonate (precursor) with acetophenone (solvent) and calcined at 200 ℃ for a very long duration of 24 hours. In comparison, our work has produced more homogeneous In_2O_3 NPs of 15 nm at 300°C for a much shortened duration of 2 hours. Besides, the particle size of In_2O_3 NPs was gradually increased when the calcination temperature was further increased from 300 to 600 ℃ in this work. It can expected that the smaller grains tend to coalesce to form bigger particles at higher calcination temperature as shown in Figure 4.18 (d, f, h and j) (Selvakumar et al., 2014).

Furthermore, it was observed that the particle size distribution seems to be more homogeneous as presented in Figure 4.18 (a and c). In contrast, it seems less homogeneous as shown in Figure 4.18 (e, i and j). In fact, both nucleation and crystal growth took place in the crystallization of In_2O_3 NPs during calcination by the rearrangement of the In_2O_3 molecules in their amorphous phase. Both nucleation and crystal growth were take place across the precipitates rather than its surfaces only. The nucleation and crystal growth of the particles were controlled when more In_2O_3 molecules were inside the precipitates as well as the slowly spreading of molecules in solid state (Pang & Bao, 2003). The relative smaller size of In_2O_3 NPs with higher crystallinity was expected to be produced. However, high surface area of NPs makes them thermodynamically unstable where they may agglomerate through Van der Waals interaction (Amirsalari & Shayesteh, 2015; Man et al., 2014). Thereby, HRTEM analysis shows that the largest size of NPs (27.67 nm) with higher crystallinity are presented in this work when the In_2O_3 NPs was calcined at 600 ℃. However, in this work, the structure properties of In_2O_3 NPs in terms of particles size have been improved where the smallest In_2O_3 NPs (14.67 nm) were formed at a lower calcination temperature of 300 ℃ via co-precipitation method.

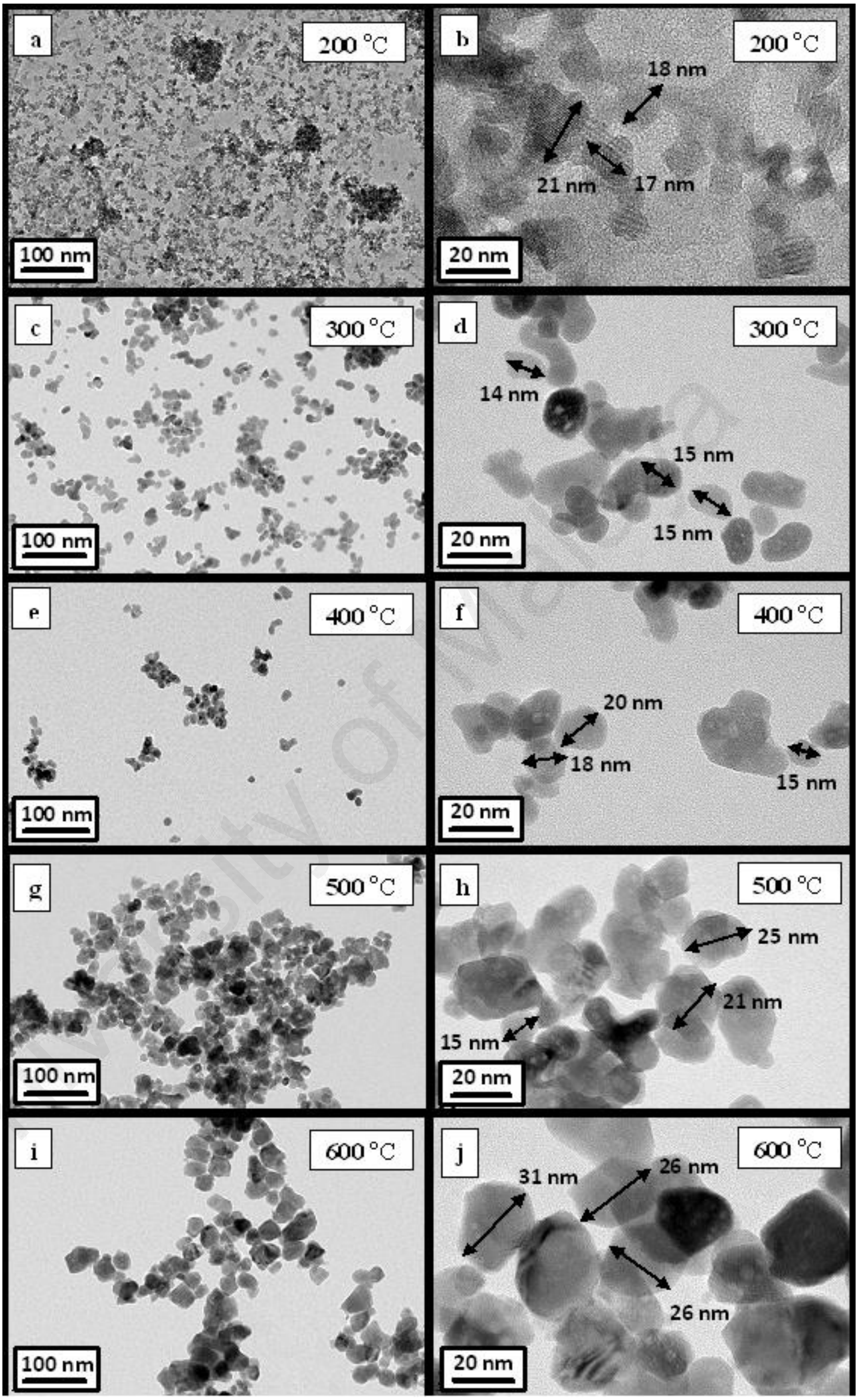

Figure 4.18: HRTEM images of In_2O_3 NPs calcined at (a and b) 200 ℃; (c and d) 300 ℃; (e and f) 400 ℃; (g and h) 500 ℃; and (i and j) 600 ℃.

CHAPTER 5

CONCLUSION AND FUTURE RECOMMENDATIONS

5.1 Introduction

This chapter presents the summary of the overall finding results on the structural properties of the as-prepared $In(OH)_3$ NPs and In_2O_3 NPs synthesized by co-precipitation method.

5.1.1 Conclusion

The principal objectives of this research have been successfully achieved. The as-prepared $In(OH)_3$ NPs and In_2O_3 NPs have been formed by co-precipitation method. The as-prepared $In(OH)_3$ NPs were initially synthesized at different pH values (8,9,10 and 11). Meanwhile, the In_2O_3 NPs were formed when the as-prepared $In(OH)_3$ NPs were calcined at different temperature of 200, 300, 400, 500 and 600 ℃. The effect of pH variation on the stability and structural properties of the as-prepared $In(OH)_3$ NPs synthesized by co-precipitation method were investigated, while the effect of the calcination temperatures on the structural properties of In_2O_3 NPs synthesized by co-precipitation method were studied. In this work, it was evidenced the smallest particles size (11.76 nm) with maximum stability (3.68 mV) of $In(OH)_3$ NPs were synthesized at pH 10 by co-precipitation. Besides, the smallest In_2O_3 NPs (14.67 nm) with well distribution were obtained at 300 ℃ in this study. As compared to previous work, this work has shown much improvement (Li et al., 2006; Xiao et al., 2016; Yang et al., 2010). By using co-precipitation method, the crystallite size of In_2O_3 NPs smaller than 20 nm were formed when the as-prepared $In(OH)_3$ NPs were synthesized at an optimum pH 10 and further calcined at a lower calcination temperature of 300 ℃. Furthermore, it was revealed that the crystallite size, stability and the morphology of In_2O_3 NPs were strongly depend on the pH of precursor solution and calcination temperature as well as the synthesis method.

5.1.2 pH variation effects

$In(OH)_3$ NPs have been successfully synthesized at pH values of 8, 9, 10 and 11 by co-precipitation method. The XRD pattern and TEM indicated all the samples synthesized at different pH values have pure cubic $In(OH)_3$ without any impurities. This result is then further supported by FTIR and Raman spectroscopy analysis, concluding that the cubic crystal structure of $In(OH)_3$ were presented in precursor solution. Furthermore, the average particles size for all samples was found having the similar trend as pH varies from 8 to 11. Based on the experimental results, it is confirms that the pH play critical roles in formation of $In(OH)_3$ NPs with different morphology, structure and size distribution. Nucleation rate and the morphology of the $In(OH)_3$ NPs may vary from one sample to another. Subsequently, the higher amount of NH_4OH is required to reach the suitable pH values of 8, 9, 10 and 11. Supersaturate solution of $In(OH)_3$ NPs at pH 10 lead to generation of small nuclei results in formation of small particles size. In conclusion, it is verified that the $In(OH)_3$ NPs synthesized at pH 10 gave the best result, owing to the smallest particles size of 11.76 nm with maximum stability of 3.68 mV. Thus, by using the same technique, further investigation of the effect of calcination temperatures on the structural properties of In_2O_3 NPs was conducted at pH 10.

5.1.3 Calcination temperatures effects

In_2O_3 NPs have been successfully prepared by calcined the as-prepared $In(OH)_3$ NPs at 200 ℃, 300 ℃, 400 ℃, 500 ℃, and 600 ℃. The XRD pattern, FTIR and Raman spectroscopy showed that $In(OH)_3$ were still arise in the samples up to 200 ℃. However, it is observed that the presence of pure In_2O_3 without any impurities in all the samples after calcined at 300 ℃ and beyond. Furthermore, HRTEM images illustrated that the rounded cubic crystal structure of In_2O_3 NPs is formed for all of the samples. It is established that the recrystallization of NPs is occurred during calcination and the NPs tend to agglomerate at higher temperature. With the calcination temperature increasing from 200 to 600 ℃, the average particles size for all the samples was found having the similar trend. These experimental results demonstrated that the calcination temperature also is a key factor in formation of In_2O_3 NPs with different morphology, structure and size distribution. The crystallinity and crystallite size of In_2O_3 NPs increased with calcination temperature represents there is an improvement of crystallite growth at higher calcination temperature. This inference can be supported by XRD, FTIR and Raman analysis which can be observed from the peak intensity. Lastly, it is concluded that the In_2O_3 NPs smaller than 20 nm which are about 14.67 nm with well particles distribution are able to form at a lower temperature of 300 ℃.

5.2 Recommendation for future research

The investigation in the present study exposed huge interesting areas that require further in-depth evaluation and future discovery. The following ideas are suggested for future research works:

i) It is worthwhile to further study on the effects of pH and calcination temperatures variations on the structural properties of the In_2O_3 NPs synthesized by other types of method such as hydrothermal, sol-gel, and solvothermal method which may able to produce an optimum In_2O_3 NPs in terms of its particles size, distribution and morphology.

ii) Calcining time-dependent experiment of In_2O_3 NPs would be interesting to carry out which may have large affect their structural properties as well as to understand the morphology evolution during the calcination process.

iii) Addition of some steric stabilizer in the precursor solution are recommended for future work which shall contribute for better particles distribution in order to improve the electrical properties of In_2O_3 NPs for gas sensing applications.

REFERENCES

Acacia, N., Barreca, F., Barletta, E., Spadaro, D., Curro, G., & Neri, F. (2010). Laser ablation synthesis of indium oxide nanoparticles in water. *Applied Surface Science, 256*(22), 6918-6922.

Addonizio, M. L., Aronne, A., Daliento, S., Tari, O., Fanelli, E., & Pernice, P. (2014). Sol-gel synthesis of ZnO transparent conductive films: The role of pH. *Applied Surface Science, 305*, 194-202.

Alias, S. S., Ismail, A. B., & Mohamad, A. A. (2010). Effect of pH on ZnO nanoparticle properties synthesized by sol-gel centrifugation. *Journal of Alloys and Compounds, 499*(2), 231-237.

Amirsalari, A., & Shayesteh, S. F. (2015). Effects of pH and calcination temperature on structural and optical properties of alumina nanoparticles. *Superlattices and Microstructures, 82*, 507-524.

Athawale, A. A., & Bapat, M. (2005). A soft solution process to synthesize nanocrystalline barium zirconate via reactive solid state precursors. *Science and Technology of Nanomaterials - ICMAT 2003, 23*, 3-6.

Atou, T., Kusaba, K., Fukuoka, K., Kikuchi, M., & Syono, Y. (1990). Shock-Induced Phase-Transition of Sc2o3-Type, Y2o3-Type, Sm2o3-Type, Gd2o3-Type, In2o3-Type Compounds. *Journal of Solid State Chemistry, 89*(2), 378-384.

Avivi, S., Mastai, Y., & Gedanken, A. (2000). Sonohydrolysis of In3+ ions: Formation of needlelike particles of indium hydroxide. *Chemistry of Materials, 12*(5), 1229-1233.

Ayeshamariam, A., Bououdina, M., & Sanjeeviraja, C. (2013). Optical, electrical and sensing properties of In2O3 nanoparticles. *Materials Science in Semiconductor Processing, 16*(3), 686-695.

Bagheri-Mohagheghi, M. M., Shahtahmasebi, N., Mozafari, E., & Shokooh-Saremi, M. (2009). Effect of the synthesis route on the structural properties and shape of the indium oxide (In2O3) nano-particles. *Physica E-Low-Dimensional Systems & Nanostructures, 41*(10), 1757-1762.

Barisik, M., Atalay, S., Beskok, A., & Qian, S. Z. (2014). Size Dependent Surface Charge Properties of Silica Nanoparticles. *Journal of Physical Chemistry C, 118*(4), 1836-1842.

Berengue, O. M., Rodrigues, A. D., Dalmaschio, C. J., Lanfredi, A. J. C., Leite, E. R., & Chiquito, A. J. (2010). Structural characterization of indium oxide nanostructures: a Raman analysis. *Journal of Physics D-Applied Physics, 43*(4).

Cantalini, C., Wlodarski, W., Sun, H. T., Atashbar, M. Z., Passacantando, M., & Santucci, S. (2000). NO2 response of In2O3 thin film gas sensors prepared by sol-gel and vacuum thermal evaporation techniques. *Sensors and Actuators B-Chemical, 65*(1-3), 101-104.

Cao, H. Q., Zheng, H., Liu, K. Y., & Fu, R. P. (2010). Single-Crystalline Semiconductor In(OH)(3) Nanocubes with Bifunctions: Superhydrophobicity and Photocatalytic Activity. *Crystal Growth & Design, 10*(2), 597-601.

Cao, S. X., Zhao, C., Han, T., & Peng, L. L. (2016). Hydrothermal synthesis, characterization and gas sensing properties of the WO3 nanofibers. *Materials Letters, 169*, 17-20.

Caruntu, D., Yao, K., Zhang, Z. X., Austin, T., Zhou, W. L., & O'Connor, C. J. (2010). One-Step Synthesis of Nearly Monodisperse, Variable-Shaped In2O3 Nanocrystals in Long Chain Alcohol Solutions. *Journal of Physical Chemistry C, 114*(11), 4875-4886.

Chand, P., Gaur, A., & Kumar, A. (2012). Structural and optical properties of ZnO nanoparticles synthesized at different pH values. *Journal of Alloys and Compounds, 539*, 174-178.

Chang, Y. C. (2014). Controlling growth of single-crystalline indium hydroxide nanocuboids with enhanced sharp cathodoluminescence peak. *Journal of Alloys and Compounds, 615*, 538-541.

Chen, J. C., Chen, W. C., Tien, Y. C., & Shih, C. J. (2010). Effect of calcination temperature on the crystallite growth of cerium oxide nano-powders prepared by the co-precipitation process. *Journal of Alloys and Compounds, 496*(1-2), 364-369.

Chen, X. T., Lu, T. C., Wei, N., Lu, Z. W., Zhang, W., Ma, B. Y., . . . Jiang, F. F. (2014). Effect of ball-milling granulation with PVB adhesive on the sinterability of co-precipitated Yb:YAG nanopowders. *Journal of Alloys and Compounds, 589*, 448-454.

Chen, Y. W., Yen, T. M., & Li, C. P. (1995). Preparation of Alumina-Zirconia Materials by the Sol-Gel Method from Metal Alkoxides. *Journal of Non-Crystalline Solids, 185*(1-2), 49-55.

Chithra, M. J., Sathya, M., & Pushpanathan, K. (2015). Effect of pH on Crystal Size and Photoluminescence Property of ZnO Nanoparticles Prepared by Chemical Precipitation Method. *Acta Metallurgica Sinica-English Letters, 28*(3), 394-404.

Choi, K. I., Kim, H. R., & Lee, J. H. (2009). Enhanced CO sensing characteristics of hierarchical and hollow In(2)O(3) microspheres. *Sensors and Actuators B-Chemical, 138*(2), 497-503.

Chung, W. Y. (2001). Gas-sensing properties of spin-coated indium oxide film on various substrates. *Journal of Materials Science-Materials in Electronics, 12*(10), 591-596.

Cukrov, L. M., Tsuzuki, T., & McCormick, P. G. (2001). SnO2 nanoparticles prepared by mechanochemical processing. *Scripta Materialia, 44*(8-9), 1787-1790.

de Vasconcelos, C. L., de Moura, K. T., Morais, W. A., Dantas, T. N. C., Pereira, M. R., & Fonseca, J. L. C. (2005). Dispersing phase viscometry and zeta potential in alumina dispersions. *Colloid and Polymer Science, 283*(4), 413-420.

Devi, P. S., Chatterjee, M., & Ganguli, D. (2002). Indium tin oxide nano-particles through an emulsion technique. *Materials Letters, 55*(4), 205-210.

Dodd, A. C., & McCormick, P. G. (2002). Synthesis of nanocrystalline ZrO2 powders by mechanochemical reaction of ZrCl4 with LiOH. *Journal of the European Ceramic Society, 22*(11), 1823-1829.

Donato, N., Neri, F., Neri, G., Latino, M., Barreca, F., Spadaro, S., . . . Curro, G. (2011). CO sensing devices based on indium oxide nanoparticles prepared by laser ablation in water. *Thin Solid Films, 520*(3), 922-926.

Elouali, S., Bloor, L. G., Binions, R., Parkin, I. P., Carmalt, C. J., & Darr, J. A. (2012). Gas Sensing with Nano-Indium Oxides (In2O3) Prepared via Continuous Hydrothermal Flow Synthesis. *Langmuir, 28*(3), 1879-1885.

Epifani, M., Siciliano, P., Gurlo, A., Barsan, N., & Weimar, U. (2004). Ambient pressure synthesis of corundum-type In2O3. *Journal of the American Chemical Society, 126*(13), 4078-4079.

Exarhos, G. J., & Zhou, X. D. (2007). Discovery-based design of transparent conducting oxide films. *Thin Solid Films, 515*(18), 7025-7052.

Fan, Y. J., Wang, S. W., & Sun, Z. X. (2012). In2O3 hollow spheres: One-step solvothermal synthesis and gas sensing properties. *Materials Chemistry and Physics, 134*(1), 93-97.

Ferrari, A. C. (2007). Raman spectroscopy of graphene and graphite: Disorder, electron-phonon coupling, doping and nonadiabatic effects. *Solid State Communications, 143*(1-2), 47-57.

Flores-Mendoza, M. A., Castanedo-Perez, R., Torres-Delgado, G., Marin, J. M., & Zelaya-Angel, O. (2008). Influence of the annealing temperature on the properties of undoped indium oxide thin films obtained by the sol-gel method. *Thin Solid Films, 517*(2), 681-685.

Forsh, E. A., Marikutsa, A. V., Martyshov, M. N., Forsh, P. A., Rumyantseva, M. N., Gaskov, A. M., & Kashkarov, P. K. (2014). Charge carrier transport mechanisms in nanocrystalline indium oxide. *Thin Solid Films, 558*, 320-325.

Fuerstenau, D. W., & Pradip. (2005). Zeta potentials in the flotation of oxide and silicate minerals. *Advances in Colloid and Interface Science, 114*, 9-26.

Gagaoudakis, E., Bender, M., Douloufakis, E., Katsarakis, N., Natsakou, E., Cimalla, V., & Kiriakidis, G. (2001). The influence of deposition parameters on room temperature ozone sensing properties of InOx films. *Sensors and Actuators B-Chemical, 80*(2), 155-161.

Gan, L. M., Zhang, K., & Chew, C. H. (1996). Preparation of silica nanoparticles from sodium orthosilicate in inverse microemulsions. *Colloids and Surfaces a-Physicochemical and Engineering Aspects, 110*(2), 199-206.

Gao, L. P., Cheng, Z. X., Xiang, Q., Zhang, Y., & Xu, J. Q. (2015). Porous corundum-type In2O3 nanosheets: Synthesis and NO2 sensing properties. *Sensors and Actuators B-Chemical, 208*, 436-443.

Gao, T., & Wang, T. H. (2006). Catalytic growth of In2O3 nanobelts by vapor transport. *Journal of Crystal Growth, 290*(2), 660-664.

Garkova, R., Volksch, G., & Russel, C. (2006). In2O3 and tin-doped In2O3 nanocrystals prepared by glass crystallization. *Journal of Non-Crystalline Solids, 352*(50-51), 5265-5270.

Goh, K. H., Haseeb, A. S. M. A., & Wong, Y. H. (2016). Physical and electrical properties of thermal oxidized Sm2O3 gate oxide thin film on Si substrate: Influence of oxidation durations. *Thin Solid Films, 606*, 80-86.

Goh, K. W., Johan, M. R., & Wong, Y. H. (2016). Effect of pH variation on the stability and structural properties of In(OH)(3) nanoparticles synthesized by co-precipitation method. *Applied Physics a-Materials Science & Processing, 122*(10).

Golan, G., Axelevitch, A., Gorenstein, B., & Peled, A. (2007). Novel type of indium oxide thin films sputtering for opto-electronic applications. *Applied Surface Science, 253*(15), 6608-6611.

Gondal, M. A., Drmosh, Q. A., & Saleh, T. A. (2010). Preparation and characterization of SnO2 nanoparticles using high power pulsed laser. *Applied Surface Science, 256*(23), 7067-7070.

Gordani, G. R., Mohseni, M., Ghasemi, A., & Hosseini, S. R. (2016). Microstructure, magnetic and microwave absorptive behavior of doped W-type hexaferrite nanoparticles prepared by co-precipitation method. *Materials Research Bulletin, 76*, 187-194.

Gu, F. B., Zhang, L., Wang, Z. H., Han, D. M., & Guo, G. S. (2014). Fine-tuning the structure of cubic indium oxide and their ethanol-sensing properties. *Sensors and Actuators B-Chemical, 193*, 669-678.

Guo, Q. X., Zhao, Y. S., Jiang, C., Mao, W. L., & Wang, Z. W. (2008). Phase transformation in Sm2O3 at high pressure: In situ synchrotron X-ray diffraction study and ab initio DFT calculation. *Solid State Communications, 145*(5-6), 250-254.

Guoa, L. J., Shen, X. P., Zhu, G. X., & Chen, K. M. (2011). Preparation and gas-sensing performance of In2O3 porous nanoplatelets. *Sensors and Actuators B-Chemical, 155*(2), 752-758.

Gupta, V. K., Agarwal, S., & Saleh, T. A. (2011). Synthesis and characterization of alumina-coated carbon nanotubes and their application for lead removal. *Journal of Hazardous Materials, 185*(1), 17-23.

Gurlo, A., Barsan, N., Weimar, U., Ivanovskaya, M., Taurino, A., & Siciliano, P. (2003). Polycrystalline well-shaped blocks of indium oxide obtained by the sol-gel method and their gas-sensing properties. *Chemistry of Materials, 15*(23), 4377-4383.

Gurlo, A., Ivanovskaya, M., Barsan, N., Schweizer-Berberich, M., Weimar, U., Gopel, W., & Dieguez, A. (1997). Grain size control in nanocrystalline In2O3 semiconductor gas sensors. *Sensors and Actuators B-Chemical, 44*(1-3), 327-333.

Gurlo, A., Ivanovskaya, M., Pfau, A., Weimar, U., & Gopel, W. (1997). Sol-gel prepared In2O3 thin films. *Thin Solid Films, 307*(1-2), 288-293.

Gurlo, A., Kroll, P., & Riedel, R. (2008). Metastability of corundum-type In2O3. *Chemistry-a European Journal, 14*(11), 3306-3310.

Guzman, K. A. D., Finnegan, M. P., & Banfield, J. F. (2006). Influence of surface potential on aggregation and transport of titania nanoparticles. *Environmental Science & Technology, 40*(24), 7688-7693.

Hafeezullah, Yamani, Z. H., Iqbal, J., Qurashi, A., & Hakeem, A. (2014). Rapid sonochemical synthesis of In2O3 nanoparticles their doping optical, electrical and hydrogen gas sensing properties. *Journal of Alloys and Compounds, 616*, 76-80.

Hamada, S., Kudo, Y., & Kobayashi, T. (1993). Precipitation of Uniform Indium Hydroxide Particles from Indium 2-Aminobutyrato Complex Solutions. *Colloids and Surfaces a-Physicochemical and Engineering Aspects, 79*(2-3), 227-232.

Han, J. T., Huang, Y. H., Wu, X. J., Wu, C. L., Wei, W., Peng, B., . . . Goodenough, J. B. (2006). Tunable synthesis of bismuth ferrites with various morphologies. *Advanced Materials, 18*(16), 2145-+.

Herrmann, M., Forter-Barth, U., Kempa, P. B., & Krober, H. (2009). Particle Characterization by X-ray Powder Diffraction. *Chemical Engineering & Technology, 32*(7), 1067-1072.

Houng, B., Huang, C. L., & Tsai, S. Y. (2007). Effect of the pH on the growth and properties of sol-gel derived boron-doped ZnO transparent conducting thin film. *Journal of Crystal Growth, 307*(2), 328-333.

Hu, J. Q., Zhu, F. R., Zhang, J., & Gong, H. (2003). A room temperature indium tin oxide/quartz crystal microbalance gas sensor for nitric oxide. *Sensors and Actuators B-Chemical, 93*(1-3), 175-180.

Hu, W. B., Tian, D. T., Mi, Y. Z., Nie, G. H., Zhao, Y. M., Liu, Z. L., & Yao, K. L. (2009). Synthesis and characterization of In2O3 nanocube via a solvothermal-calcination route. *Materials Chemistry and Physics, 118*(2-3), 277-280.

Husain, S., Alkhtaby, L. A., Bhat, I., & Khan, W. (2015). Effect of pH variation on structural and optical properties of Zn0.95Co0.05O nanoparticles. *Journal of Luminescence, 160*, 311-316.

Jeong, J. S., Lee, J. Y., Lee, C. J., An, S. J., & Yi, G. C. (2004). Synthesis and characterization of high-quality In2O3 nanobelts via catalyst-free growth using a simple physical vapor deposition at low temperature. *Chemical Physics Letters, 384*(4-6), 246-250.

Jiang, X. C., Wang, Y. L., Herricks, T., & Xia, Y. N. (2004). Ethylene glycol-mediated synthesis of metal oxide nanowires. *Journal of Materials Chemistry, 14*(4), 695-703.

Jiao, Z., Wu, M. H., Gu, J. Z., & Sun, X. L. (2003). The gas sensing characteristics of ITO thin film prepared by sol-gel method. *Sensors and Actuators B-Chemical, 94*(2), 216-221.

Jin, M., Kim, J. W., Kim, J. M., Jurng, J., Bae, G. N., Jeon, J. K., & Park, Y. K. (2011). Effect of calcination temperature on the oxidation of benzene with ozone at low temperature over mesoporous alpha-Mn2O3. *Powder Technology, 214*(3), 458-462.

Jonsson, B., Nonat, A., Labbez, C., Cabane, B., & Wennerstrom, H. (2005). Controlling the cohesion of cement paste. *Langmuir, 21*(20), 9211-9221.

Kam, K. C., Deepak, F. L., Cheetham, A. K., & Rao, C. N. R. (2004). In2O3 nanowires, nanobouquets and nanotrees. *Chemical Physics Letters, 397*(4-6), 329-334.

Kim, D. W., Kodama, S., Sekiguchi, H., & Park, D. W. (2014). Preparation of indium oxide powders by microwave plasma dehydration of indium hydroxide powders. *Advanced Powder Technology, 25*(1), 261-266.

Kim, D. W., Oh, S. G., & Lee, J. D. (1999). Preparation of ultrafine monodispersed indium-tin oxide particles in AOT-based reverse microemulsions as nanoreactors. *Langmuir, 15*(5), 1599-1603.

Kim, J. M., Park, J. K., Kim, K. N., Kim, C. H., & Jang, H. G. (2006). Synthesis of In2O3 nano-materials with various shapes. *Current Applied Physics, 6*, E198-E201.

Kim, T. Y., Jang, H. M., & Cho, S. M. (2001). Short-ranged clusters with tetragonal symmetry in La-modified PbTiO3 relaxor ferroelectrics. *Solid State Communications, 119*(8-9), 527-532.

Kohli, N., Singh, O., & Singh, R. C. (2011). Influence of pH on particle size and sensing response of chemically synthesized chromium oxide nanoparticles to alcohols. *Sensors and Actuators B-Chemical, 158*(1), 259-264.

Konkena, B., & Vasudevan, S. (2012). Understanding Aqueous Dispersibility of Graphene Oxide and Reduced Graphene Oxide through pK(a) Measurements. *Journal of Physical Chemistry Letters, 3*(7), 867-872.

Korotcenkov, G., Brinzari, V., Cerneavschi, A., Ivanov, M., Golovanov, V., Cornet, A., . . . Arbiol, J. (2004). The influence of film structure on In2O3 gas response. *Thin Solid Films, 460*(1-2), 315-323.

Kukushkin, S. A., & Nemna, S. V. (2001). The effect of pH on nucleation kinetics in solutions. *Doklady Physical Chemistry, 377*(4-6), 117-120.

Kuo, C. Y., Lu, S. Y., & Wei, T. Y. (2005). In2O3 nanorod formation induced by substrate structure. *Journal of Crystal Growth, 285*(3), 400-407.

Labbez, C., Jonsson, B., Skarba, M., & Borkovec, M. (2009). Ion-Ion Correlation and Charge Reversal at Titrating Solid Interfaces. *Langmuir, 25*(13), 7209-7213.

Lau, L. N., Ibrahim, N. B., & Baqiah, H. (2015). Influence of precursor concentration on the structural, optical and electrical properties of indium oxide thin film prepared by a sol-gel method. *Applied Surface Science, 345*, 355-359.

Lee, C. H., Kim, M., Kim, T., Kim, A., Paek, J., Lee, J. W., . . . Lee, K. (2006). Ambient pressure syntheses of size-controlled corundum-type In2O3 nanocubes. *Journal of the American Chemical Society, 128*(29), 9326-9327.

Lee, M. H., Oh, S. G., Yi, S. C., Seo, D. S., Hong, J. P., Kim, C. O., . . . Yoo, J. S. (2000). Characterization of Eu-doped Y2O3 nanoparticles prepared in nonionic reverse microemulsions in relation to their application for field emission display. *Journal of the Electrochemical Society, 147*(8), 3139-3142.

Lei, Z. B., Ma, G. J., Liu, M. Y., You, W. S., Yan, H. J., Wu, G. P., . . . Li, C. (2006). Sulfur-substituted and zinc-doped In(OH)(3): A new class of catalyst for photocatalytic H-2 production from water under visible light illumination. *Journal of Catalysis, 237*(2), 322-329.

Lewis, B. G., & Paine, D. C. (2000). Applications and processing of transparent conducting oxides. *Mrs Bulletin, 25*(8), 22-27.

Li, B. X., Xie, Y., Jing, M., Rong, G. X., Tang, Y. C., & Zhang, G. Z. (2006). In2O3 hollow microspheres: Synthesis from designed in (OH)(3) precursors and applications in gas sensors and photocatalysis. *Langmuir, 22*(22), 9380-9385.

Li, D., Cheng, X. W., Yu, X. J., & Xing, Z. P. (2015). Preparation and characterization of TiO2-based nanosheets for photocatalytic degradation of acetylsalicylic acid: Influence of calcination temperature. *Chemical Engineering Journal, 279*, 994-1003.

Li, H., Arita, T., Takami, S., & Adschiri, T. (2011). Rapid synthesis of tin-doped indium oxide microcrystals in supercritical water using hydrazine as reducing agent. *Progress in Crystal Growth and Characterization of Materials, 57*(4), 117-126.

Li, S. T., Qiao, X. L., Chen, H. G., Wang, H. S., Jia, F., & Qiu, X. L. (2006). Effects of temperature on indium tin oxide particles synthesized by co-precipitation. *Journal of Crystal Growth, 289*(1), 151-156.

Li, Y., Wang, J. X., Feng, B., Duan, K., & Weng, J. (2015). Synthesis and characterization of antimony-doped tin oxide (ATO) nanoparticles with high conductivity using a facile ammonia-diffusion co-precipitation method. *Journal of Alloys and Compounds, 634*, 37-42.

Lin, L. T., Tang, L., Zhang, R., Deng, C., Chen, D. J., Cao, L. W., & Meng, J. X. (2015). Monodisperse In2O3 nanoparticles synthesized by a novel solvothermal method with In(OH)(3) as precursors. *Materials Research Bulletin, 64*, 139-145.

Lin, Z. J., Zhu, Q., Dong, Y., Liu, S. H., Li, J. G., Li, X. D., . . . Sun, X. D. (2016). Synthesis and formation mechanisms of morphology-controllable indium-containing precursors and optical properties of the derived In2O3 particles. *Crystengcomm, 18*(21), 3768-3776.

Liu, C. L., Zhang, H. X., Komarneni, S., & Pantano, C. G. (1994). Porous Silicon Oxycarbide Glasses from Organically Modified Silica Gels of High Surface Area. *Journal of Sol-Gel Science and Technology, 1*(2), 141-151.

Liu, D., Lei, W. W., Zou, B., Yu, S. D., Hao, J., Wang, K., . . . Zou, G. T. (2008). High-pressure x-ray diffraction and Raman spectra study of indium oxide. *Journal of Applied Physics, 104*(8).

Liu, X. H., Zhou, L. B., Yi, R., Zhang, N., Shi, R. R., Gao, G. H., & Qiu, G. Z. (2008). Single-Crystalline Indium Hydroxide and Indium Oxide Microcubes: Synthesis and Characterization. *Journal of Physical Chemistry C, 112*(47), 18426-18430.

Lopez-Quintela, M. A. (2003). Synthesis of nanomaterials in microemulsions: formation mechanisms and growth control. *Current Opinion in Colloid & Interface Science, 8*(2), 137-144.

Lupan, O., Cretu, V., Postica, V., Ababii, N., Polonskyi, O., Kaidas, V., . . . Adelung, R. (2016). Enhanced ethanol vapour sensing performances of copper oxide nanocrystals with mixed phases. *Sensors and Actuators B-Chemical, 224*, 434-448.

Malik, M. A., Wani, M. Y., & Hashim, M. A. (2012). Microemulsion method: A novel route to synthesize organic and inorganic nanomaterials. *Arabian Journal of Chemistry, 5*(4), 397-417.

Man, J., Zhang, S., Li, J. F., Zhao, B., & Chen, Y. (2014). Effects of electrolyte pH on morphologies and mechanical properties of alpha-Al2O3/Ni composite coatings and role of zeta potentials in co-deposition process. *Surface & Coatings Technology, 249*, 118-124.

Meyer, C., Sanchez, J. P., Thomasson, J., & Itie, J. P. (1995). Mossbauer and Energy-Dispersive X-Ray-Diffraction Studies of the Pressure-Induced Crystallographic Phase-Transition in C-Type Yb2o3. *Physical Review B, 51*(18), 12187-12193.

Minami, T. (2008). Present status of transparent conducting oxide ing oxide thin-film development for Indium-Tin-Oxide (ITO) substitutes. *Thin Solid Films, 516*(17), 5822-5828.

Mitsui, T., Matsui, T., Kikuchi, R., & Eguchi, K. (2009). Microstructural Transformation with Heat-Treatment of Aluminum Hydroxide with Gibbsite Structure. *Bulletin of the Chemical Society of Japan, 82*(5), 618-623.

Mittemeijer, E. J., & Welzel, U. (2008). The "state of the art" of the diffraction analysis of crystallite size and lattice strain. *Zeitschrift Fur Kristallographie, 223*(9), 552-560.

Mote, V. D., Purushotham, Y., & Dole, B. N. (2011). Structural and morphological studies on Mn substituted ZnO nanometer-sized crystals. *Crystal Research and Technology, 46*(7), 705-710.

Motta, F. V., Lima, R. C., Marques, A. P. A., Leite, E. R., Varela, J. A., & Longo, E. (2010). In2O3 microcrystals obtained from rapid calcination in domestic microwave oven. *Materials Research Bulletin, 45*(11), 1703-1706.

Motta, F. V., Lima, R. C., Marques, A. P. A., Li, M. S., Leite, E. R., Varela, J. A., & Longo, E. (2010). Indium hydroxide nanocubes and microcubes obtained by microwave-assisted hydrothermal method. *Journal of Alloys and Compounds, 497*(1-2), L25-L28.

Mudunkotuwa, I. A., & Grassian, V. H. (2010). Citric Acid Adsorption on TiO2 Nanoparticles in Aqueous Suspensions at Acidic and Circumneutral pH: Surface Coverage, Surface Speciation, and Its Impact on Nanoparticle-Nanoparticle Interactions. *Journal of the American Chemical Society, 132*(42), 14986-14994.

Naono, H., & Nakai, K. (1989). Thermal-Decomposition of Gamma-Feooh Fine Particles. *Journal of Colloid and Interface Science, 128*(1), 146-156.

Niederberger, M., Garnweitner, G., Buha, J., Polleux, J., Ba, J. H., & Pinna, N. (2006). Nonaqueous synthesis of metal oxide nanoparticles: Review and indium oxide as case study for the dependence of particle morphology on precursors and solvents. *Journal of Sol-Gel Science and Technology, 40*(2-3), 259-266.

Oh, S. Y., Yoo, D. I., Shin, Y., Kim, H. C., Kim, H. Y., Chung, Y. S., . . . Youk, J. H. (2005). Crystalline structure analysis of cellulose treated with sodium hydroxide and carbon dioxide by means of X-ray diffraction and FTIR spectroscopy. *Carbohydrate Research, 340*(15), 2376-2391.

Ovanesyan, Z., Aljzmi, A., Almusaynid, M., Khan, A., Valderrama, E., Nash, K. L., & Marucho, M. (2016). Ion-ion correlation, solvent excluded volume and pH effects on physicochemical properties of spherical oxide nanoparticles. *Journal of Colloid and Interface Science, 462*, 325-333.

Palomino, D., & Stoll, S. (2013). Fulvic acids concentration and pH influence on the stability of hematite nanoparticles in aquatic systems. *Journal of Nanoparticle Research, 15*(2).

Pandya, S. G., Corbett, J. P., Jadwisienczak, W. M., & Kordesch, M. E. (2016). Structural characterization and X-ray analysis by Williamson-Hall method for Erbium doped Aluminum Nitride nanoparticles, synthesized using inert gas condensation technique. *Physica E-Low-Dimensional Systems & Nanostructures, 79*, 98-102.

Pang, Y. X., & Bao, X. (2003). Influence of temperature, ripening time and calcination on the morphology and crystallinity of hydroxyapatite nanoparticles. *Journal of the European Ceramic Society, 23*(10), 1697-1704.

Parast, M. S. Y., & Morsali, A. (2011). Sonochemical-assisted synthesis of nano-structured indium(III) hydroxide and oxide. *Ultrasonics Sonochemistry, 18*(1), 375-381.

Patel, S. K. S., Dewangan, K., Srivastav, S. K., & Gajbhiye, N. S. (2014). Synthesis of monodisperse In2O3 nanoparticles and their d(0) ferromagnetism. *Current Applied Physics, 14*(6), 905-908.

Perez-Maqueda, L. A., Wang, L. F., & Matijevic, E. (1998). Nanosize indium hydroxide by peptization of colloidal precipitates. *Langmuir, 14*(16), 4397-4401.

Pettibone, J. M., Cwiertny, D. M., Scherer, M., & Grassian, V. H. (2008). Adsorption of organic acids on TiO2 nanoparticles: Effects of pH, nanoparticle size, and nanoparticle aggregation. *Langmuir, 24*(13), 6659-6667.

Pramanik, N. C., Das, S., & Biswas, P. K. (2002). The effect of Sn(IV) on transfonnation of co-precipitated hydrated In(III) and Sn(IV) hydroxides to indium tin oxide (ITO) powder. *Materials Letters, 56*(5), 671-679.

Rani, S., Suri, P., Shishodia, P. K., & Mehra, R. M. (2008). Synthesis of nanocrystalline ZnO powder via sol-gel route for dye-sensitized solar cells. *Solar Energy Materials and Solar Cells, 92*(12), 1639-1645.

Reddy, C. V., Vattikuti, S. V. P., Ravikumar, R. V. S. S. N., Moon, S. J., & Shim, J. (2015). Influence of calcination temperature on Cd0.3Co0.7Fe2O4 nanoparticles: Structural, thermal and magnetic properties. *Journal of Magnetism and Magnetic Materials, 394*, 70-76.

Ruiz-Agudo, C., Putnis, C. V., Ruiz-Agudo, E., & Putnis, A. (2015). The influence of pH on barite nucleation and growth. *Chemical Geology, 391*, 7-18.

Safi, R., Ghasemi, A., Shoja-Razavi, R., Ghasemi, E., & Sodaee, T. (2016). Rietveld structure refinement, cations distribution and magnetic features of CoFe2O4 nanoparticles synthesized by co-precipitation, hydrothermal, and combustion methods. *Ceramics International, 42*(5), 6375-6382.

Safi, R., Ghasemi, A., Shoja-Razavi, R., & Tavousi, M. (2015). The role of pH on the particle size and magnetic consequence of cobalt ferrite. *Journal of Magnetism and Magnetic Materials, 396*, 288-294.

Sajjia, M., Benyounis, K. Y., & Olabi, A. G. (2012). The simulation and optimization of heat treatment of cobalt ferrite nanoparticles prepared by the sol-gel technique. *Powder Technology, 222*, 143-151.

Sankhla, A., Sharma, R., Yadav, R. S., Kashyap, D., Kothari, S. L., & Kachhwaha, S. (2016). Biosynthesis and characterization of cadmium sulfide nanoparticles - An emphasis of zeta potential behavior due to capping. *Materials Chemistry and Physics, 170*, 44-51.

Sasaki, T., Shimizu, Y., & Koshizaki, N. (2006). Preparation of metal oxide-based nanomaterials using nanosecond pulsed laser ablation in liquids. *Journal of Photochemistry and Photobiology a-Chemistry, 182*(3), 335-341.

Sathish, S., Shekar, B. C., & Nataraj, D. (2014). Synthesis and characterization of indium aluminate (InAlO3) nanoparticles by wet chemical method. *Advanced Powder Technology, 25*(3), 1007-1015.

Schmitt, J., & Flemming, H. C. (1998). FTIR-spectroscopy in microbial and material analysis. *International Biodeterioration & Biodegradation, 41*(1), 1-11.

Seetha, M., Bharathi, S., Raj, A. D., Mangaaraj, D., & Nataraj, D. (2009). Optical investigations on indium oxide nano-particles prepared through precipitation method. *Materials Characterization, 60*(12), 1578-1582.

Seetha, M., Meena, P., Mangalaraj, D., Masuda, Y., & Senthil, K. (2012). Synthesis of indium oxide cubic crystals by modified hydrothermal route for application in room temperature flexible ethanol sensors. *Materials Chemistry and Physics, 133*(1), 47-54.

Selvakumar, D., Dharmaraj, N., Kadirvelu, K., Kumar, N. S., & Padaki, V. C. (2014). Effect of sintering temperature on structural and optical properties of indium(III) oxide nanoparticles prepared with Triton X-100 by hydrothermal method. *Spectrochimica Acta Part a-Molecular and Biomolecular Spectroscopy, 133*, 335-339.

Shao, F., Hernandez-Ramirez, F., Prades, J. D., Fabrega, C., Andreu, T., & Morante, J. R. (2014). Copper (II) oxide nanowires for p-type conductometric NH3 sensing. *Applied Surface Science, 311*, 177-181.

Sharma, P. K., Jilavi, M. H., Varadan, V. K., & Schmidt, H. (2002). Influence of initial pH on the particle size and fluorescence properties of the nano scale Eu(III) doped yttria. *Journal of Physics and Chemistry of Solids, 63*(1), 171-177.

Shi, Z., Wang, W., & Zhang, Z. K. (2008). Synthesis and characterization of indium hydroxide truncated polyhedral microcrystals. *Materials Letters, 62*(27), 4293-4295.

Shukla, S., Seal, S., Ludwig, L., & Parish, C. (2004). Nanocrystalline indium oxide-doped tin oxide thin film as low temperature hydrogen sensor. *Sensors and Actuators B-Chemical, 97*(2-3), 256-265.

Singh, V. N., & Mehta, B. R. (2003). A two-step synthesis procedure for In2O3 nanoparticle films having well-defined particle size. *Japanese Journal of Applied Physics Part 1-Regular Papers Short Notes & Review Papers, 42*(7a), 4226-4232.

Sivakami, R., Dhanuskodi, S., & Karvembu, R. (2016). Estimation of lattice strain in nanocrystalline RuO2 by Williamson-Hall and size-strain plot methods. *Spectrochimica Acta Part a-Molecular and Biomolecular Spectroscopy, 152*, 43-50.

Sohnel, O. (1982). Electrolyte Crystal Aqueous-Solution Interfacial-Tensions from Crystallization Data. *Journal of Crystal Growth, 57*(1), 101-108.

Song, K. C., & Kim, J. H. (1999). Preparation of nanosize tin oxide particles from water-in-oil microemulsions. *Journal of Colloid and Interface Science, 212*(1), 193-196.

Song, P. Y., & Zhang, W. D. (2014). Controlled synthesis and gas sensing properties of In2O3 with different phases from urchin-like InOOH microspheres. *Materials Research Bulletin, 53*, 177-184.

Souza, C. C., Rey, J. F. Q., & Muccillo, E. N. S. (2009). Synthesis and characterization of spherical and narrow size distribution indium oxide nanoparticles. *Applied Surface Science, 255*(6), 3779-3783.

Stathatos, E., Lianos, P., DelMonte, F., Levy, D., & Tsiourvas, D. (1997). Formation of TiO2 nanoparticles in reverse micelles and their deposition as thin films on glass substrates. *Langmuir, 13*(16), 4295-4300.

Tahar, R. B. H., Ban, T., Ohya, Y., & Takahashi, Y. (1997). Optical, structural, and electrical properties of indium oxide thin films prepared by the sol-gel method. *Journal of Applied Physics, 82*(2), 865-870.

Tang, S. C., Yao, J. S., Chen, J., & Luo, J. G. (2003). Preparation of indium tin oxide (ITO) with a single-phase structure. *Journal of Materials Processing Technology, 137*(1-3), 82-85.

Tao, X. J., Zhao, Y. B., Sun, L., & Zhou, S. M. (2015). One-pot low temperature solvothermal synthesis of In2O3 and InOOH nanostructures. *Materials Chemistry and Physics, 149*, 275-281.

Tavares, M. T. S., Lovisa, L. X., Araujo, V. D., Longo, E., Li, M. S., Nascimento, R. M., . . . Motta, F. V. (2014). Fast photocatalytic degradation of an organic dye and photoluminescent properties of Zn doped In(OH)(3) obtained by the microwave-assisted hydrothermal method. *Materials Science in Semiconductor Processing, 27*, 1036-1041.

Thanh, N. T. K., Maclean, N., & Mahiddine, S. (2014). Mechanisms of Nucleation and Growth of Nanoparticles in Solution. *Chemical Reviews, 114*(15), 7610-7630.

Tong, P. V., Hoa, N. D., Duy, N. V., Le, D. T. T., & Hieu, N. V. (2016). Enhancement of gas-sensing characteristics of hydrothermally synthesized WO3 nanorods by surface decoration with Pd nanoparticles. *Sensors and Actuators B-Chemical, 223*, 453-460.

Trotta, M., Cavalli, R., Ugazio, E., & Gasco, M. R. (1996). Phase behaviour of microemulsion systems containing lecithin and lysolecithin as surfactants. *International Journal of Pharmaceutics, 143*(1), 67-73.

Tseng, T. T., & Tseng, W. J. (2009). Effect of polyvinylpyrrolidone on morphology and structure of In2O3 nanorods by hydrothermal synthesis. *Ceramics International, 35*(7), 2837-2844.

Tshabalala, P., Motaung, D. E., Mhlongoa, G. H., & Ntwaeaborwa, O. M. (2016). Facile synthesis of improved room temperature gas sensing properties of TiO2 nanostructures: Effect of acid treatment. *Sensors and Actuators B-Chemical, 224*, 841-856.

Tsuji, T., Hamagami, T., Kawamura, T., Yamaki, J., & Tsuji, M. (2005). Laser ablation of cobalt and cobalt oxides in liquids: influence of solvent on composition of prepared nanoparticles. *Applied Surface Science, 243*(1-4), 214-219.

Vaidya, S., Ahmad, T., Agarwal, S., & Ganguli, A. K. (2007). Nanocrystalline oxalate/carbonate precursors of Ce and Zr and their decompositions to CeO(2) and ZrO(2) nanoparticles. *Journal of the American Ceramic Society, 90*(3), 863-869.

Vasiliev, R. B., Rumyantseva, M. N., Dorofeev, S. G., Potashnikova, Y. M., Ryabova, L. I., & Gaskov, A. M. (2004). Crystallite size effect on the conductivity of the ultradisperse ceramics of SnO2 and In2O3. *Mendeleev Communications, 14*(4), 167-169.

Venkateswarlu, K., Bose, A. C., & Rameshbabu, N. (2010). X-ray peak broadening studies of nanocrystalline hydroxyapatite by Williamson-Hall analysis. *Physica B-Condensed Matter, 405*(20), 4256-4261.

Vijayaprasath, G., Murugan, R., Asaithambi, S., Sakthivel, P., Mahalingam, T., Hayakawa, Y., & Ravi, G. (2016). Structural and magnetic behavior of Ni/Mn co-doped ZnO nanoparticles prepared by co-precipitation method. *Ceramics International, 42*(2), 2836-2845.

Vives, S., Gaffet, E., & Meunier, C. (2004). X-ray diffraction line profile analysis of iron ball milled powders. *Materials Science and Engineering a-Structural Materials Properties Microstructure and Processing, 366*(2), 229-238.

Wahab, R., Ansari, S. G., Kim, Y. S., Song, M., & Shin, H. S. (2009). The role of pH variation on the growth of zinc oxide nanostructures. *Applied Surface Science, 255*(9), 4891-4896.

Wahab, R., Kim, Y. S., & Shin, H. S. (2009). Synthesis, Characterization and Effect of pH Variation on Zinc Oxide Nanostructures. *Materials Transactions, 50*(8), 2092-2097.

Wan, P., Yang, W., Wang, X. N., Hu, J. M., & Zhang, H. (2015). Reduced graphene oxide modified with hierarchical flower-like In(OH)(3) for NO2 room-temperature sensing. *Sensors and Actuators B-Chemical, 214*, 36-42.

Wang, J. C., Zhang, F., Wang, Y. J., Luo, G. S., & Cai, W. B. (2016). A size-controllable preparation method for indium tin oxide particles using a membrane dispersion micromixer. *Chemical Engineering Journal, 293*, 1-8.

Wang, X. Q., Zhang, M. F., Liu, J. Y., Luo, T., & Qian, Y. T. (2009). Shape- and phase-controlled synthesis of In2O3 with various morphologies and their gas-sensing properties. *Sensors and Actuators B-Chemical, 137*(1), 103-110.

Widodo, S., & Sudrajad, N. (2015). Synthesis of Indium Oxide (In2O3) Nano Particles Using Sol Gel Method as Active Material on Gas Sensor. *Proceedings of the 2014 International Conference on Physics and Its Applications*, 171-175.

Xiao, B. X., Wang, F., Zhai, C. B., Wang, P., Xiao, C. H., & Zhang, M. Z. (2016). Facile synthesis of In2O3 nanoparticles for sensing properties at low detection temperature. *Sensors and Actuators B-Chemical, 235*, 251-257.

Xu, H. R., & Yu, A. B. (2007). Synthesis and sintering of tin-doped indium oxide nanoparticles with uniform size. *Materials Letters, 61*(19-20), 4043-4045.

Xu, J., Chen, Y., & Shen, J. (2008). Ethanol sensor based on hexagonal indium oxide nanorods prepared by solvothermal methods. *Materials Letters, 62*(8-9), 1363-1365.

Xu, J. Q., Chen, Y. P., Pan, Q. Y., Xiang, Q., Cheng, Z. X., & Dong, X. W. (2007). A new route for preparing corundum-type In2O3 nanorods used as gas-sensing materials. *Nanotechnology, 18*(11).

Xu, J. Q., Wang, X. H., & Shen, J. N. (2006). Hydrothermal synthesis of In2O3 for detecting H2S in air. *Sensors and Actuators B-Chemical, 115*(2), 642-646.

Xu, X. X., & Wang, X. (2009). Size- and Surface-Determined Transformations: From Ultrathin InOOH Nanowires to Uniform c-In2O3 Nanocubes and rh-In2O3 Nanowires. *Inorganic Chemistry, 48*(8), 3890-3895.

Yang, H., Irudayaraj, J., & Paradkar, M. M. (2005). Discriminant analysis of edible oils and fats by FTIR, FT-NIR and FT-Raman spectroscopy. *Food Chemistry, 93*(1), 25-32.

Yang, H. M., Tang, A. D., Zhang, X. C., Yang, W. G., & Qiu, G. Z. (2004). In2O3 nanoparticles synthesized by mechanochemical processing. *Scripta Materialia, 50*(4), 413-415.

Yang, H. X., Yang, Z. J., Liang, H., Liu, L., Guo, J. X., & Yang, Y. Z. (2010). Solvothermal synthesis of In(OH)(3) nanorods and their conversion to In2O3. *Materials Letters, 64*(13), 1418-1420.

Yang, J., Cheng, H. F., Martens, W. N., & Frost, R. L. (2011). Application of Infrared Emission Spectroscopy to the Thermal Transition of Indium Hydroxide to Indium Oxide Nanocubes. *Applied Spectroscopy, 65*(1), 113-118.

Yang, J., Frost, R. L., & Martens, W. N. (2010). Thermogravimetric analysis and hot-stage Raman spectroscopy of cubic indium hydroxide. *Journal of Thermal Analysis and Calorimetry, 100*(1), 109-116.

Yao, F., Wu, Q. L., Lei, Y., Guo, W. H., & Xu, Y. J. (2008). Thermal decomposition kinetics of natural fibers: Activation energy with dynamic thermogravimetric analysis. *Polymer Degradation and Stability, 93*(1), 90-98.

Yin, W. Y., Su, J., Cao, M. H., Ni, C. Y., Cloutier, S. G., Huang, Z. G., . . . Wei, B. Q. (2009). In(OH)(3) and In2O3 Micro/Nanostructures: Controllable NaOAc-Assisted Microemulsion Synthesis and Raman Properties. *Journal of Physical Chemistry C, 113*(45), 19493-19499.

Yu, D. B., Yu, S. H., Zhang, S. Y., Zuo, J., Wang, D. B., & Qian, Y. T. (2003). Metastable hexagonal In2O3 nanofibers templated from InOOH nanofibers under ambient pressure. *Advanced Functional Materials, 13*(6), 497-501.

Yuan, H., Xu, M., & Huang, Q. Z. (2014). Effects of pH of the precursor sol on structural and optical properties of Cu-doped ZnO thin films. *Journal of Alloys and Compounds, 616*, 401-407.

Yuan, H., Zhang, L., Xu, M., & Du, X. S. (2015). Effect of sol pH on microstructures, optical and magnetic properties of (Co,Fe)-codoped ZnO films synthesized by sol-gel method. *Journal of Alloys and Compounds, 651*, 571-577.

Zhan, Z. L., Song, W. H., & Jiang, D. G. (2004). Preparation of nanometer-sized In2O3 particles by a reverse microemulsion method. *Journal of Colloid and Interface Science, 271*(2), 366-371.

Zhang, A. C., Zhang, Z. H., Chen, J. J., Sheng, W., Sun, L. S., & Xiang, J. (2015). Effect of calcination temperature on the activity and structure of MnOx/TiO2 adsorbent for Hg-0 removal. *Fuel Processing Technology, 135*, 25-33.

Zhang, H., Yang, D., Ma, X. Y., Ji, Y. J., Xu, J., & Que, D. L. (2004). Synthesis of flower-like ZnO nanostructures by an organic-free hydrothermal process. *Nanotechnology, 15*(5), 622-626.

Zhang, L., He, R., & Gu, H. C. (2006). Oleic acid coating on the monodisperse magnetite nanoparticles. *Applied Surface Science, 253*(5), 2611-2617.

Zhang, W., Tan, Y. Y., Gao, Y. L., Wu, J. X., Hu, J. B., He, S. Y., . . . Tang, B. H. J. (2015). In2O3 Nanoparticles on Three-Dimensionally Ordered Macroporous (3DOM) Carbon for Pseudocapacitor Electrodes. *Electrochimica Acta, 176*, 861-867.

Zhang, X. H., Xie, S. Y., Ni, Z. M., Zhang, X., Jiang, Z. Y., Xie, Z. X., . . . Zheng, L. S. (2003). Controllable growth of In(OH)(3) nanorods with rod-in-rod structure in a surfactant solution. *Inorganic Chemistry Communications, 6*(12), 1445-1447.

Zheng, X. B., Li, X. H., Huang, Z. J., Zhang, B., Wang, Z. X., Guo, H. J., & Yang, Z. H. (2015). Enhanced electrochemical performance of LiNi0.6Co0.2Mn0.2O2 cathode materials by ultrasonic-assisted co-precipitation method. *Journal of Alloys and Compounds, 644*, 607-614.

Zhou, H. J., Cai, W. P., & Zhang, L. D. (1999). Synthesis and structure of indium oxide nanoparticles dispersed within pores of mesoporous silica. *Materials Research Bulletin, 34*(6), 845-849.

Zhu, H., Wang, X. L., Wang, Z. J., Yang, C., Yang, F., & Yang, X. R. (2008). Self-assembled 3D microflowery In(OH)(3) architecture and its conversion to In2O3. *Journal of Physical Chemistry C, 112*(39), 15285-15292.

Zhu, H. L., Wang, Y., Wang, N. Y., Li, Y., & Yang, J. (2004). Hydrothermal synthesis of indium hydroxide nanocubes. *Materials Letters, 58*(21), 2631-2634.

Zhu, H. L., Yao, K. H., Zhang, H., & Yang, D. R. (2005). InOOH hollow spheres synthesized by a simple hydrothermal reaction. *Journal of Physical Chemistry B, 109*(44), 20676-20679.

Zhuang, Z. B., Peng, Q., Liu, J. F., Wang, X., & Li, Y. D. (2007). Indium hydroxides, oxyhydroxides, and oxides nanocrystals series. *Inorganic Chemistry, 46*(13), 5179-5187.

LIST OF PUBLICATIONS AND PAPERS PRESENTED

Goh K.W., Mohd R.J., Wong Y.H., *Effect of pH variation on the stability and structural properties of* $In(OH)_3$ *nanoparticles synthesized by co-precipitation method.* Applied Physics A-Materials Science & Processing, 2016. **122**(2). (Published)

Goh K.W., Mohd R.J., Wong Y.H., *Enhanced structural properties of* In_2O_3 *Nanoparticles at lower calcination temperature synthesized by co-precipitation method.* Micro & Nano Letters, 2017. (Under review)